A PUMP-ASSISTED CAPILLARY LOOP EVAPORATOR DESIGN FOR HIGH HEAT-FLUX DISSIPATION

by

Silvia Anali Soto de la Torre

A Thesis

Submitted to the Faculty of Purdue University

In Partial Fulfillment of the Requirements for the degree of

Master of Science in Mechanical Engineering

School of Mechanical Engineering

West Lafayette, Indiana

December 2021

THE PURDUE UNIVERSITY GRADUATE SCHOOL
STATEMENT OF COMMITTEE APPROVAL

Dr. Justin A. Weibel, Chair

School of Mechanical Engineering

Dr. Davide Ziviani

School of Mechanical Engineering

Dr. Shripad T. Revankar

School of Nuclear Engineering

Approved by:

Dr. Nicole Key

Para mi familia.

Sin importar la distancia, me acompañan siempre.

ACKNOWLEDGMENTS

I would like to thank Professor Justin A. Weibel for all the support and guidance throughout this journey, for the invaluable feedback, and for always ensuring that the best was always delivered. I am also thankful with my review committee, Professor Davide Ziviani and Professor Shripad Revankar for their time and feedback that led to the success of this work.

I thank my parents, my brother, and my sister for their love and encouragement to always pursue my dreams and fulfill my goals. I thank my colleagues from the Cooling Technologies Research Center, for all their help in my work, and companionship through my time at Purdue: Srivathsan Sudhakar, Rishav Roy, Saeel Pai, Matthew Clark, Serdar Ozguc, Manohar Bongarala, Soumya Bandyopadhyay, Julian Castillo, Maureen Winter, Sara Lyons, Debraliz Isaac, Haotian Liu, and Tayler Shelly.

I also acknowledge the financial support provided by the Toyota Research Institute of North America, and members of the Cooling Technologies Research Center (CTRC), a graduated NSF Industry/University Cooperative Research Center at Purdue University.

TABLE OF CONTENTS

LIST OF TABLES

LIST OF FIGURES

NOMENCLATURE

Abbreviations

AAR	Area Availability Ratio
CHF	Critical Heat Flux
CPL	Capillary Pump Loop
EV	Electric Vehicles
ID	Inner Diameter
LHP	Loop Heat Pipe
OD	Outer Diameter
PACL	Pumped-Assisted Capillary Loop
PF	Porosity Fraction
VC	Vapor Chamber

Nomenclature

A	Area (m^2)
D	Diameter (m)
D_{pore}	Mean pore diameter (m)
h	Height (m)
h_{fg}	Heat of vaporization (J/kg)
K	Permeability (m^2)
k	Thermal conductivity (W/mK)
$\dot{m}$	Mass flow rate (kg/s)
N_{post}	Total number of posts
n	Number of posts in $n \times n$ array
l	Length (m)
P	Pressure (Pa)
Q	Heat input (W)
r	Radius (m) /radial coordinate
s	Center-to-center center tube spacing
t	Thickness (m)
u	Velocity (m/s)
x_{boil}	Fraction area available for boiling
z	Axial coordinate

Greek Symbols

ρ	Density (kg/m^3)
ϕ	Porosity (-)
σ	Surface Tension (N/m)
μ	Dynamic viscosity (kg/m-s)
ν	Kinematic viscosity (m^2/s)

Subscripts

boil	Boiling
c	Capillary
cap	Wick's cap layer
eff	Effective
evap	Evaporator
in	Inlet
l	Liquid
max	Maximum
part	Particle
post	Feeding post (porous or solid)
v	Vapor
wick	Base wick

ABSTRACT

Passive two-phase cooling devices such as capillary pump loops, loop heat pipes, and vapor chambers can utilize capillary-fed boiling in the porous evaporator wick to achieve high heat flux dissipation, while maintaining low thermal resistances. These systems typically rely only on passive capillary pumping through the porous wick to transport fluid. This inevitably leads to limits on the maximum heat flux and power dissipation based on the maximum capillary pressure available. To overcome these capillary pumping limitations in these passive devices, a mechanical pump can be added to the system to create a pump-assisted capillary loop (PACL). The pump can actively transport the fluid to overcome the pressure drop in liquid lines, reserving all of the available capillary action to draw liquid from a compensation chamber into the porous evaporator at the location of the heat input.

Previous studies on pump-assisted capillary loops have used a porous pathway to draw liquid to the heated evaporator surface from a liquid supply in the compensation chamber. This pathway typically comprises porous posts distributed over the heated surface area to ensure uniform liquid feeding during boiling and to avoid dryout regions. This thesis presents an evaporator design for a pump-assisted capillary loop system featuring a non-porous manifold connection between the compensation chamber and the evaporator wick base where boiling occurs. By using this approach, microscale liquid-feeding features can be implemented without the manufacturing restrictions associated with the use of porous wick pathways (such as sintered powder copper particles).

An analytical model for two-phase pressure drop prediction in the base wick is developed and used to define the evaporator geometry and feeding structure dimensions. A parametric analysis of the evaporator geometry is performed with the target of achieving a maximum heat dissipation of 1 kW/cm^2 without a capillary limit. A 24×24 microtube array configuration with an outside tube diameter of 0.25 mm was identified as a result of this analysis. This manifold delivers liquid the base wick manufactured from sintered copper particles with a mean particle diameter of 90 μm.

The resulting evaporator geometry was translated into a manufacturable copper manifold design. A modular test section design consisting of a cover for attachment of fittings, a support structure for holding the manifold, a sintered copper wick base, and a carrier plate was created and

manufactured, to accommodate for future testing scheduled to be performed by an external industry partner. The resulting design provides a testing vehicle to investigate the effect of different tubing arrangements and dimensions, as well as multiple base wick configurations. This knowledge can be used to engineer future evaporator architectures for enhanced performance. The improved understanding providing on the effect of liquid feeding distribution into the base wick, the effects of boiling on the base wick pressure drop, and the manufacturing limitations can each improve the performance prediction of evaporators with top feeding.

1. INTRODUCTION & LITERATURE REVIEW

1.1 Background and Introduction

The heat dissipation demand placed on electronics cooling systems has ever-growing requirements with the constant evolution toward smaller and higher power devices. For this reason, thermal management of electronic systems is needed for a diverse set of industry applications, such as in electric vehicles (EV), data centers, and portable electronics, among others.

To ensure that the proper operation and reliability of these electronic devices, adequate thermal management must be in place to maintain the electronics within specified temperature limits. Laloya *et al.* [1] provided a state of the art review of heat management in power electronics. They compared several thermal management techniques across different transfer mechanisms (i.e., solid, gas, liquid, or two-phase). The peak power, efficiency, cost, and power density capacity were also discussed for the different technologies, based on their maturity level.

In one urgent application, the demand for information technology systems is outpacing the capacity and capability for a sustainable energy management [2]. The technology industry has relied on the use of air-cooling technology due to its simplicity, overall low operating cost, and strong adaptability. While the objective is to increase the power dissipation from systems, the implementation of liquid cooling requires additional components such as cooling distributing units (CDUs), manifolds, and quick disconnects [3], which can together rapidly increase the cost of its implementation. For this reason, the limitations of air cooling (and how to overcome some of them) have been studied extensively [4]–[6].

Some of the factors leading to the growth of electric vehicles are the lowered cost of batteries, the consumer perception regarding the recognition of advantages, and global urbanization [7]. However, the use of batteries and their associated on-board power electronics have called for different cooling strategies and thermal management implementation in the cars. Xia *et al.* [8] presented a review of the thermal management for electric vehicle battery applications. They highlight that close to 40% of the reviewed references had been published in a span of 5 years prior to their publication, showing an increase of interest in investigating and reporting information about this subject. Siddique *et al.* [9] presented a review for thermal management strategies and limitations for phase change materials and thermoelectric coolers.

The need to have alternatives for high heat flux applications has resulted in a vast analysis and comparison between technologies such as single-phase systems (i.e., microchannel cold plates and jet impingement) and two-phase systems such as microchannel flow boiling and capillary-fed structures (i.e., vapor chambers and capillary loops [10]–[12]). Additionally operational enhancements such as coated surfaces and different wick types have been investigated [13].

Recent work has shown that pump-assisted capillary loops can provide a good alternative for heat dissipation by combining: the high heat transfer coefficient provided by boiling, without the instabilities that come with a pumped two-phase loop; the advantages of capillary-fed boiling from passive evaporators, such as a vapor chamber or loop heat pipes; and low pumping power consumption when compared to other mechanically pumped systems. A qualitative comparison summary between these systems is presented in Table 1.1

Table 1.1. Qualitative comparison of single- and two-phase (passive and active) cooling loops.

	Cooling System			
	Pumped Single-Phase Loop	**Pumped Two-Phase Loop**	**Capillary Two-Phase Loop**	**Pump-Assisted Capillary Two-Phase Loop**
Flow Rate and Pumping Power	+ (needs high flow rate)	++ (only at high vapor quality)	++++ (entirely passive)	+++ (pump only as needed)
Flow Stability and Control	++++ (simplest)	+ (instabilities)	++ (startup concerns)	+++ (like single phase)
Thermal Resistance, Temperature Uniformity, & Maximum Heat Flux	++ (non-uniform temperatures)	++++ (highest potential)	++ (capillary limited dryout heat flux)	+++ (possibly overcoming capillary limit)

Single-phase loops rely on a mechanical pump to push fluid through the heat sink device (e.g., micro-channel heat sinks or cold plates). The pump-assisted capillary pump system offers a low pumping power and low flow rate option because the liquid flow rate can be adjusted to feed only the liquid as needed based on the heat input. Therefore, a lower pumping power is required when compared to a single-phase loop, which only relies on mechanical pumping to deliver the liquid. While the pump power consumption can vary depending on the pump type, working fluid

and power dissipation of the system, pump power requirements as low as 0.3 W for systems dissipating 200 W using water have been reported [14].

Pumped two-phase loops are prone to instabilities in heated microchannels, such as static instabilities (i.e., Ledinegg instability) [15]–[19] and dynamic instabilities (such as rapid bubble growth [20], [21] or pressure drop oscillations [22]–[24]) due to the system interaction with upstream compressible volume. On the other hand, single-phase loops can be easily controlled and lack of the unpredictability of pumped two-phase flow instabilities. Even though the pump-assisted capillary loop has vapor generation due to capillary-fed boiling, separated lines are used to transport the liquid and vapor, thus removing the instability concern.

Single-phase pumped loops present the lowest temperature uniformity during operation; this because the liquid flows through the heatsink or cold plate the fluid experiences a sensible temperature rise within the heatsink. This non-uniformity results in higher thermal resistances. Due to its single-phase nature, single-phase loops also have the lowest heat transfer coefficient, when compared to other passive or active two-phase systems.

The following subsections provide a detailed review of the operation and recent literature on passive and pump-assisted two-phase cooling devices. First, entirely passive devices such as capillary pumped loops (CPL), loop heat pipes (LHP), and vapor chambers (VC) are reviewed in Section 1.2, as these have found widespread use in the past to dissipate high heat fluxes while maintaining low thermal resistances. Next, Section 1.3 provides an overview of the pumped-assisted capillary loop (PACL), its similarities and differences to the entirely passive devices, and current studies that have been performed. Lastly, the above thermal management technologies all rely on the fundamental process of capillary-fed boiling for their operation, which is also introduced in Section 1.4. The context of this background introduction and literature review is used to identify the scope and specific objectives of this thesis in Section 1.5.

1.2 Vapor Chambers, Loop Heat Pipes and Capillary Pump Loops

Vapor chambers (VC) are a closed loop cooling solution that relies on capillary action to dissipate heat from a localized heated surface area and spread it over a larger heat rejection area. A diagram representing the vapor chamber operation and the primary transport mechanisms is shown in Figure 1.1. At the evaporator, the heat input is absorbed via the phase change of the working fluid. At high heat fluxes, this may occur through boiling in the wick structure. The

generated vapor takes the heat and releases it into the rejection surface, or condenser portion, of the vapor chamber, which usually has a heat sink attached. Once the working fluid is back in a liquid form, the capillary wicking action within the pores of a wick lining the walls returns it into the heated area for the cycle to continue.

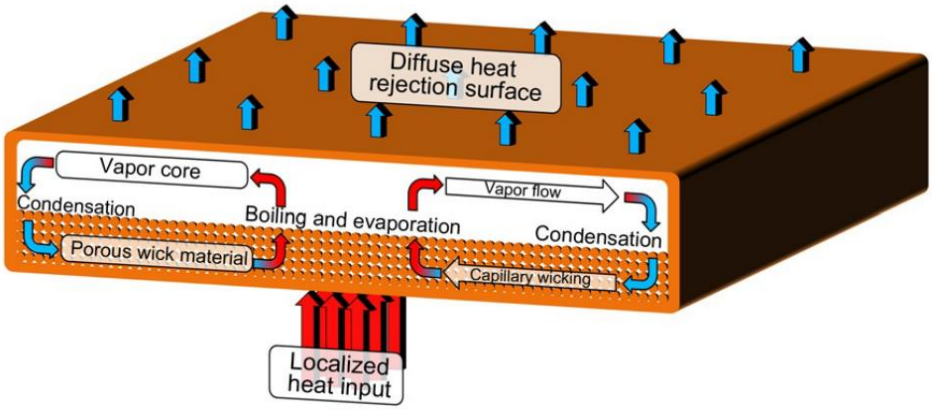

Figure 1.1. Schematic diagram for the vapor chamber operation. [13]

One of the limitations and challenges of this cooling solution is the liquid resupply by capillary forces. For the resupply to happen, liquid needs to be transported and overcome the pressure drop along the wick from the condenser or liquid return region. An inability to replenish the heated area with liquid faster than it evaporates leads to dry-out zones and sharp temperature increase; the heat input at which this occurs is called a capillary limit.

The effects of different geometric parameters and evaporator characteristics such as wick type, particle size, base thickness, etc. have been investigated in the past. Li *et al.* [25] investigated the effects of wick thickness in evaporation and boiling using sintered isotropic copper mesh evaporators. They found the boiling incipience superheat is reduced in capillary-fed boiling compared to pool boiling, resulting in lower thermal resistances; they also reported an increase in the critical heat flux with an increase in wick thickness. Li and Peterson [26] presented the effects of other wick parameters (i.e., the porosity and mesh size) on CHF. They reported an optimum porosity depending on the wick thickness and mesh size.

A particular challenge associated with boiling, which causes a large pressure drop within the evaporator wick, is to continue liquid feeding at high heat fluxes over large heat input areas.

The liquid layer present in the wick becomes thinner as it gets closer to the center of the heat input region until it finally a local dryout occurs at the center due to the lack of liquid resupply. One solution to increase this maximum heat fluxes was presented by Sudhakar *et al.* [27]. They proposed a two-layer evaporator wick, using a thin base wick layer to minimize the evaporation/boiling thermal resistance, while having a second top layer that allows liquid to return to the base through the addition of vertical feeding porous posts evenly distributed across the wick base layer. Additionally, venting posts were included in the second wick layer to allow vapor to escape from the boiling region and not block the liquid pathway. This previous work is of particular relevance due to the focus on high heat flux operation and capillary fed boiling, the desired regime of operation for the CAPL evaporator design in this work.

Other two-phase systems that utilize capillary action to passively dissipate heat are the loop heat pipes (LHP) and capillary pumped loops (CPL). For these systems, a heat source is applied into an evaporator wick. Like a vapor chamber, these systems use capillary action to retrieve the fluid from the heat source to the heat sink (condenser region) without any mechanical parts; however, instead of being intended for local heat spreading like a vapor chamber, these devices typically have evaporators and condensers that may be long distances and connected with tubes/pipes, similar to a conventionally pumped loop. While LHP and CPL are very similar in their main components that comprise them, they have different specific characteristics and arrangements. Nikitkin and Cullimore [28] described the similarities and differences between both systems. Both systems comprise an evaporator, a condenser, a reservoir or compensation chamber, and transport lines (Figure 1.2). A differentiating aspect between them is the positioning of the reservoir or compensation chamber and how it is connected to the evaporator. In a CPL, the reservoir is attached to the evaporator via the liquid line, making the evaporator a “three-port” design (Figure 1.2 (a)). The LHP has a capillary connection between the compensation chamber and the evaporator (Figure 1.2 (b)).

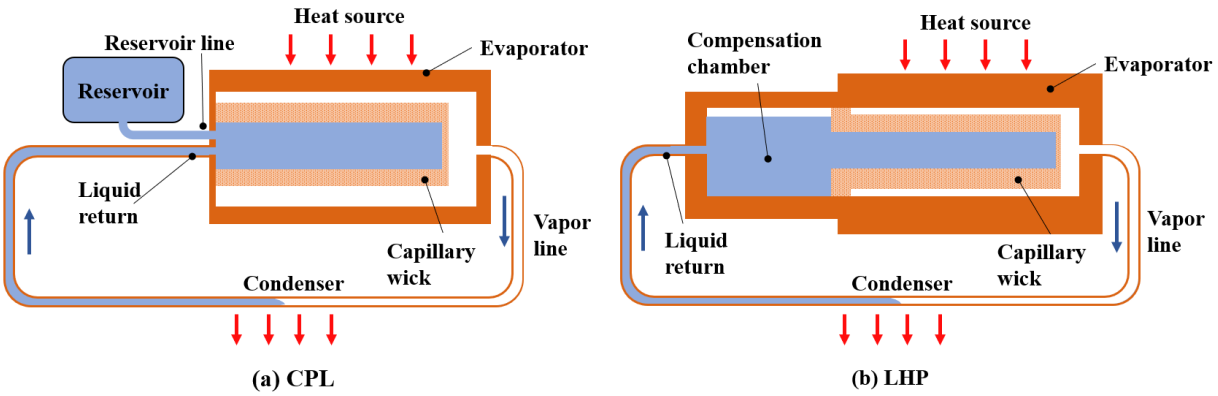

Figure 1.2. Comparison between the components and their positioning in a (a) CPL system and an (b) LHP system.

The startup process for these passive systems has been studied in the past [29]–[32]. Additionally, multiple literature review articles are available covering conventional loop heat pipes. Siedel *et al.* [33] go through an extensive review of steady-state models for LHPs developed between 1999 and 2014. The different characteristics of each of the models developed were listed and classified. Additionally, Launay and Vallée [34] focused on summarizing the experimental studies performed on loop heat pipes from 1998 to 2010. They divided their classification depending on the type of evaporator, vapor grooves, condenser, analysis (i.e., steady or transient), and investigation parameters.

1.3 Pump-Assisted Capillary Loops

One of the limitations of a purely passive system as noted in Section1.2 such as the LHP/CPL, is the power limitation imposed by the maximum available capillary pressure of the wick. In the first demonstration of a particular alternative approach to exceed this limit, Ku and Kroliczek [9] added an active mechanical component (i.e., a pump) into a system that was previously configured for passive operation. The pump was placed upstream in the liquid line connected to wicked evaporators operating in parallel. Anhydrous ammonia was used as the working fluid in this system. The evaporator outlet consisted of only the vapor lines. The vapor was condensed using a heat exchanger, with the liquid outlet pumped back into the evaporator feeding lines. Using this system,

the authors demonstrated that it was feasible and practical for increasing the power dissipation compared to the passive system.

Such systems that use an active mechanical element to pump fluid through the system, in addition to the available capillary action in the evaporator wick, have gained significant recent attention in the literature. Of note, the terminology used for these systems is varied throughout the literature, with names including a hybrid capillary pumped loop, pumped-assisted capillary-driven two-phase loop, hybrid loop heat pipe, or mechanical capillary driven two-phase loop; for consistency, this thesis adopts the term pump-assisted capillary loop (PACL) for description of these systems. Besides the evaporator and a pump, other components comprising a PACL system include a reservoir to supply liquid into the system and a heat exchanger or condenser to reject the heat from the vapor line before it is returned into the reservoir (with a typical arrangement as illustrated Figure 1.3).

Both cylindrical and flat evaporators have been studied for pump-assisted capillary loops. Schematics of both such evaporator geometries and their key components are presented in Figure 1.4. Setyawan *et al.* [14] investigated a PACL system with a cylindrical evaporator. The authors used a diaphragm pump to overcome the dry-out problem by turning the pump on during experiments and assisting the fluid transport back into the evaporator. Liu *et al.* [30] experimentally studied the startup process of a PACL system with a flat evaporator. Crepinsek and Park [35], [36] performed multiple experimental studies on a flat evaporator fed with vertical porous posts, focusing on the system's behavior at different heating conditions, as well as the operation of a PACL system with multiple evaporators placed in series and in parallel. Lee and Park [37] developed an integrated analytical system model for a PACL with a single flat evaporator.

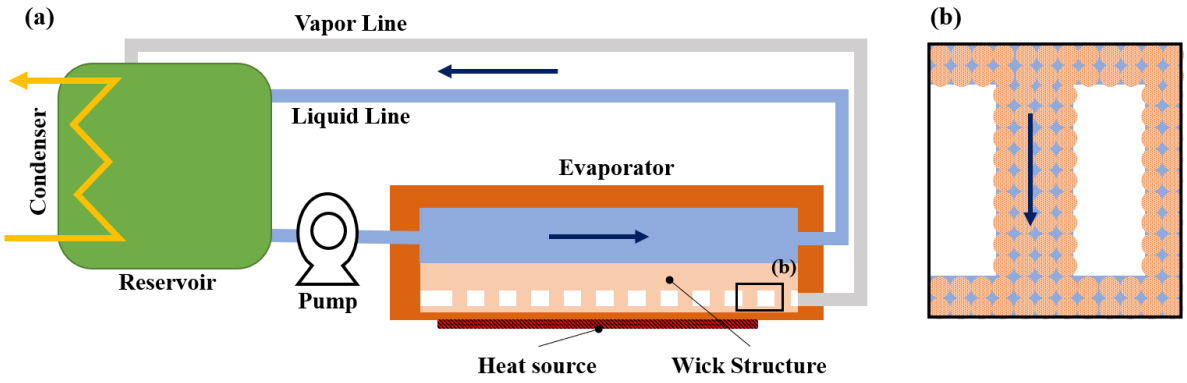

Figure 1.3. (a) PACL system diagram with a flat evaporator and condenser embedded in the reservoir. (b) Zoomed inset of the wick structure on the evaporator.

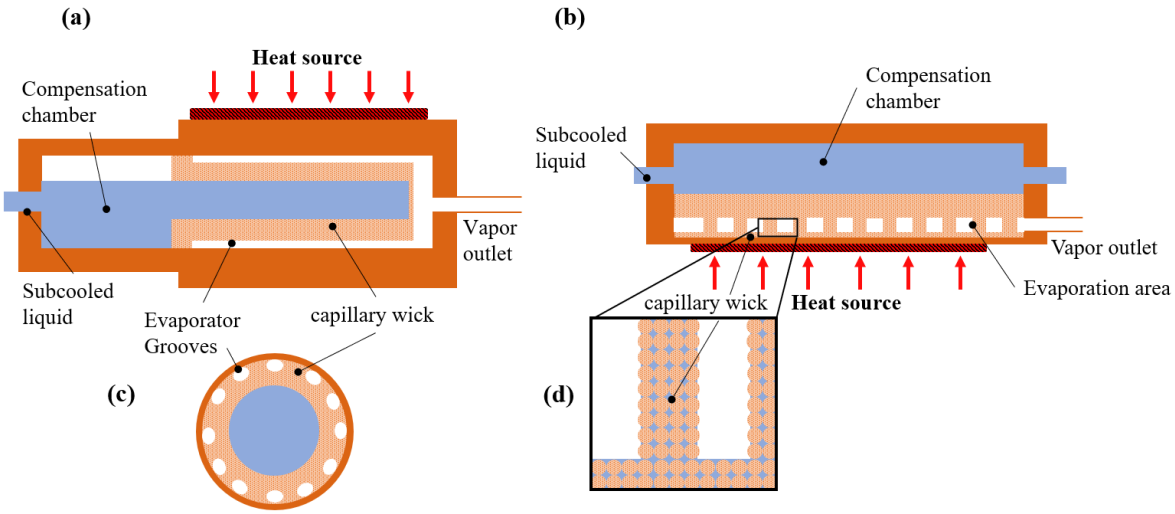

Figure 1.4. (a) Schematic diagram for a cylindrical evaporator with (c) groove and wick details. (b) Schematic diagram for a flat evaporator with (d) wick details.

1.4 Capillary-Fed Boiling

Boiling occurs when the temperature of a wetted surface exceeds the liquid saturation temperature for a given pressure [38]. When operating inside a constrained volumetric space (i.e., within the wick's pores), the bubble formation due to nucleate boiling impedes the return path for liquid to rewet the heated surface, resulting in premature evaporator dryout. To prevent boiling from happening, a heat flux operation limit has been defined in literature as a function of the

effective thermal conductivity of the wick, the wall temperature, and the critical superheat [39]. However, in some porous wick structures having many tortuous liquid pathways, the occurrence of boiling does not necessarily cause immediate dryout, and a so-called 'capillary-fed boiling' process can be maintained [13]. Smirnov [40] proposed a mechanistic heat transfer theory for boiling in capillary-porous structures, in which vapor columns are formed during boiling, and the porous surface is left with a thin liquid film. Ranjan *et al.* [41] investigated the bubble growth dynamics in a capillary wick structure for isotropic and anisotropic particle arrangements. They observed that instead of single bubble departure, vapor columns were formed through the wick structure. The mechanistic difference between pool boiling (i.e., when the sample is fully submerged in liquid), and capillary-fed boiling are presented in Figure 1.5 for increasing heat fluxes.

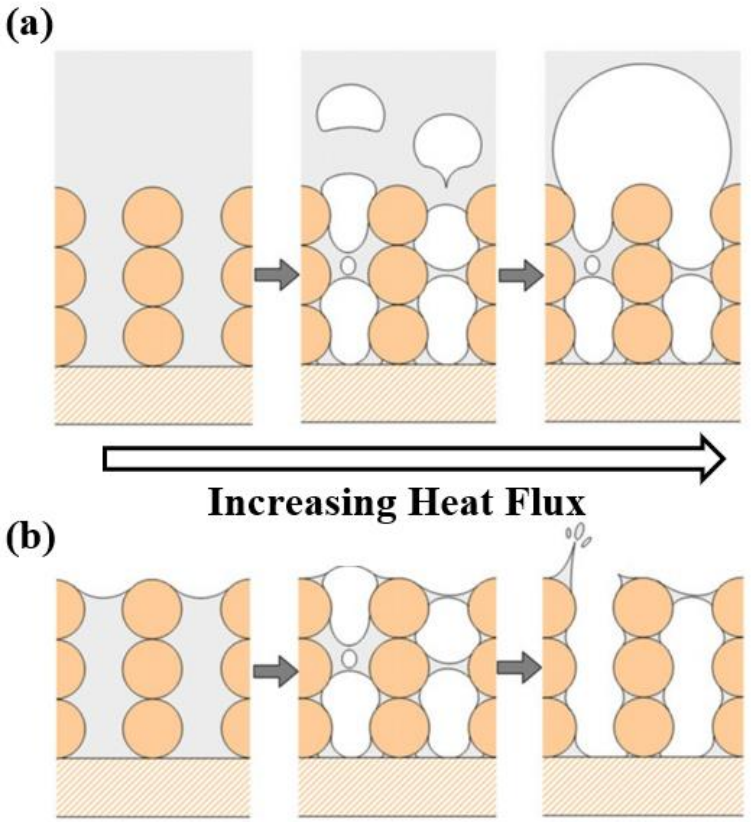

Figure 1.5. (a) Schematic representation for pool boiling for a sintered particle porous wick. (b) Schematic representation for capillary-fed boiling for a sintered particle porous wick. [13]

Weibel *et al*. [42] developed a testing facility to experimentally evaluate sintered wicks with particle diameters ranging from 600 μm to 1200 μm under conditions that replicated capillary-fed systems such as vapor chambers. They observed a reduction in the evaporator thermal resistance at the transition from evaporation to boiling mode. For enhanced capillary-fed boiling, different wick structures have been studied to understand the critical heat flux (CHF). Some of the porous structures experimentally tested for boiling performance enhancement include copper sintered particles [42], carbon-nanotube-coated surfaces [43], and copper inverse opals [17], [46]. Palko *et al.* [47] demonstrated the high heat flux dissipation capability for two-phase heat transfer in sintered copper inverse opal structures at low super heat. A comprehensive summary of recent experimental investigations performed on capillary-fed boiling is presented in Ref.[13].

Sudhakar *et. al.* [48] proposed a reduced-order analytical approach for the two-phase pressure drop in a wick while boiling. An investigation of the boiling behavior and dry-out limits was also studied in Ref. [49]. They successfully extended the dry-out heat flux by implementing an array of feeding posts delivering liquid to the boiling base wick through a two-layer wick architecture. The effect on the dry-out heat flux limit due to boiling of the array density for the feeding features, and the venting hole geometry was then studied in Ref. [50].

1.5 Scope and Objectives of this Thesis

While several works were identified in the literature review above that investigated the operational aspects of a PACL (for both flat and cylindrical evaporators), to the author's knowledge, no work could be found that explore the evaporator wick design and feeding features to enhance the system's maximum heat dissipation. For this reason, it is the objective of this work to explore, design, and manufacture a novel evaporator architecture, focused on the flat evaporator geometry. The developed design is manufacturable for future testing of this application.

This thesis is organized in five chapters. Chapter 1 provided an introduction and literature review of passive and active capillary-driven systems. Chapter 2 compares different proposed flat evaporator architectures using reduced-order model. Chapter 3 presents the results of the model-base analysis, which dictates the evaporator design to be manufactured. Chapter 4 describes the characteristics and design of the evaporator, test section, and flow loop for testing. Chapter 5 provides the conclusions and suggestions for future work.

2. EVAPORATOR CONCEPTS AND MODELING APPROACH

A flat evaporator model is considered for this design due to the compatibility it provides for cooling of electronics packages. Having a flat bottom surface (which can be mechanically finished to control the flatness and roughness) allows for direct attachment of a heat-generating device (i.e., the electronic component). This provides a better contact between both surfaces, reducing contact resistance in the case where dry contact is required, or provides an adequate surface to attach a thermal interface material to improve the heat transfer path between the electronic device and the evaporator.

Evaporators with two different feeding post structures are analyzed and compared in this work: an evaporator with porous post structures below a porous cap layer, and an evaporator with a solid manifold with microtubes running vertically from the compensation chamber to the base wick. A cross-sectional comparison diagram for both architectures is presented in Figure 2.1.

Single-phase liquid is fed through one side of the evaporator and into the compensation chamber (the liquid inlet/outlet can also be located on the lateral sides of the evaporator). For the porous post architecture, within the compensation chamber the liquid can either be drawn to the heated surface through the wetting/porous the cap layer below, or it can bypass the evaporator and exit through a liquid outlet on the compensation chamber. This configuration allows the evaporator to passively draw only the liquid that is needed for evaporation based on the heat load. For the microtubes architecture, no porous connection exists between the compensation chamber and the base. Instead, liquid is being pumped through these microtubes aided by the system pump located upstream (refer to Figure 1.3 for reference). In the route where the liquid is delivered from the compensation chamber, it passes into the base wick evaporator via feeding posts (which can have various layouts and constructions). A heat source is applied to the base, causing evaporation or capillary-boiling that generates vapor. The vapor generated due to boiling then exits the evaporator through a separated line. Aside from the feeding mechanism of liquid into the base, both concepts share the same characteristics as shown in the side-by-side comparison presented in Figure 2.1, specifically their separated lines for liquid and vapor, and the liquid being fed into the same base wick.

While both architectures provide a solution for distributed feeding to small regions at the base wick, the solid microtube architecture is proposed because the porous post diameters have a

restricted minimum size - as a general rule, it is not recommended to have a post diameter of less than three particles (e.g., 0.3 mm diameter for ~100 μm particles) for mechanical integrity and to ensure a continuous capillary pathway through the structure. Another inherent advantage of the microtubes concept is that the mechanically pressurized compensation chamber forces liquid into the tubes, and hence capillary feeding only needs to overcome the pressure drop within the base wick (versus needing to overcome the pressure through the porous posts as well).

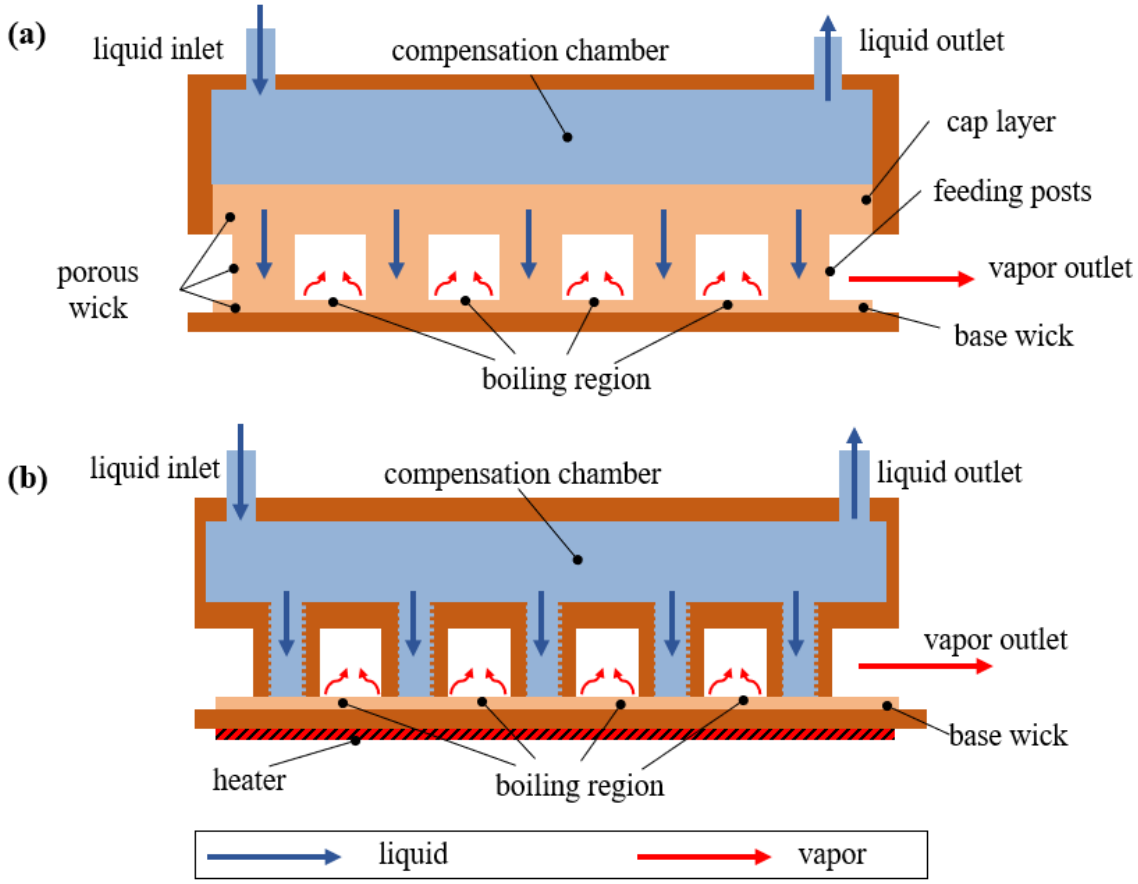

Figure 2.1. (a) Cross-sectional view of a flat evaporator using porous posts as feeding structures. (b) Cross-sectional view of a flat evaporator using microtubes for liquid feeding into the porous base wick.

2.1 Evaporator with Porous Posts

Previous studies on pump-assisted capillary loops have used evaporators with a fully porous pathway to draw liquid axially from the compensation chamber into the heated surface [51].

Typically, this pathway consists of an array of porous posts distributed over the heated surface to ensure proper liquid distribution and feeding during evaporation to avoid dry-out regions. A similar case, where porous posts were used to providing liquid to a large heated area having high heat fluxes that induced capillary fed boiling, was studied by Sudhakar *et al*. [27]. In their work that focused on evaporators for vapor chambers, a slight difference from PACLs is that the liquid source is drawn radially through the cap layer rather than above from a compensation chamber. However, the distribution of liquid into the posts and base wick area is otherwise identical to the operation in a PACL. Each of the posts can be viewed as a repeating unit that delivers liquid to the base wick, which then must pump the liquid up to an effective radius away from the post base radius. The effective radius r_{eff} is calculated by equating the circular area to which the liquid will be delivered by a post, over the area of each feeding cell as per

$$\pi r_{eff}^2 = \frac{l_{evap}^2}{N_{posts}} \tag{1}$$

A graphical representation of a feeding cell is shown in Figure 2.2 (a)

To predict the maximum heat input that induces a capillary limit, analytical models are developed and presented for the pressure drop through this sequence of porous regions as described. Figure 2.2 shows the representation of a single cell to be fed by a post, as well as the relevant parameters for the pressure drop model that was developed with the location of the geometric parameters relevant to the pressure drop model that was developed. It is assumed that the liquid mass flow rate to the base wick is completely vaporized and therefore is directly related to the heat input as per

$$\dot{m}_{total} = \frac{Q_{in}}{h_{fg}} \tag{2}$$

The pressure drops in the cap layer and the posts are calculated assuming a uniform axial flow through a porous cylindrical column with thickness t_{cap} and t_{post} respectively, as

$$\Delta P_{cap} = \frac{\nu_l \dot{m}_{post}}{\pi r_{post}^2 K} t_{cap} \tag{3}$$

$$\Delta P_{post} = \frac{\nu_l \dot{m}_{post}}{\pi r_{post}^2 K} t_{post} \tag{4}$$

where ν_l represents the kinematic viscosity of the liquid and $\dot{m}_{post}$ represents the liquid delivered per post and obtained by dividing the total mass flow rate obtained from Equation 2 by the total number of posts N_{post}.

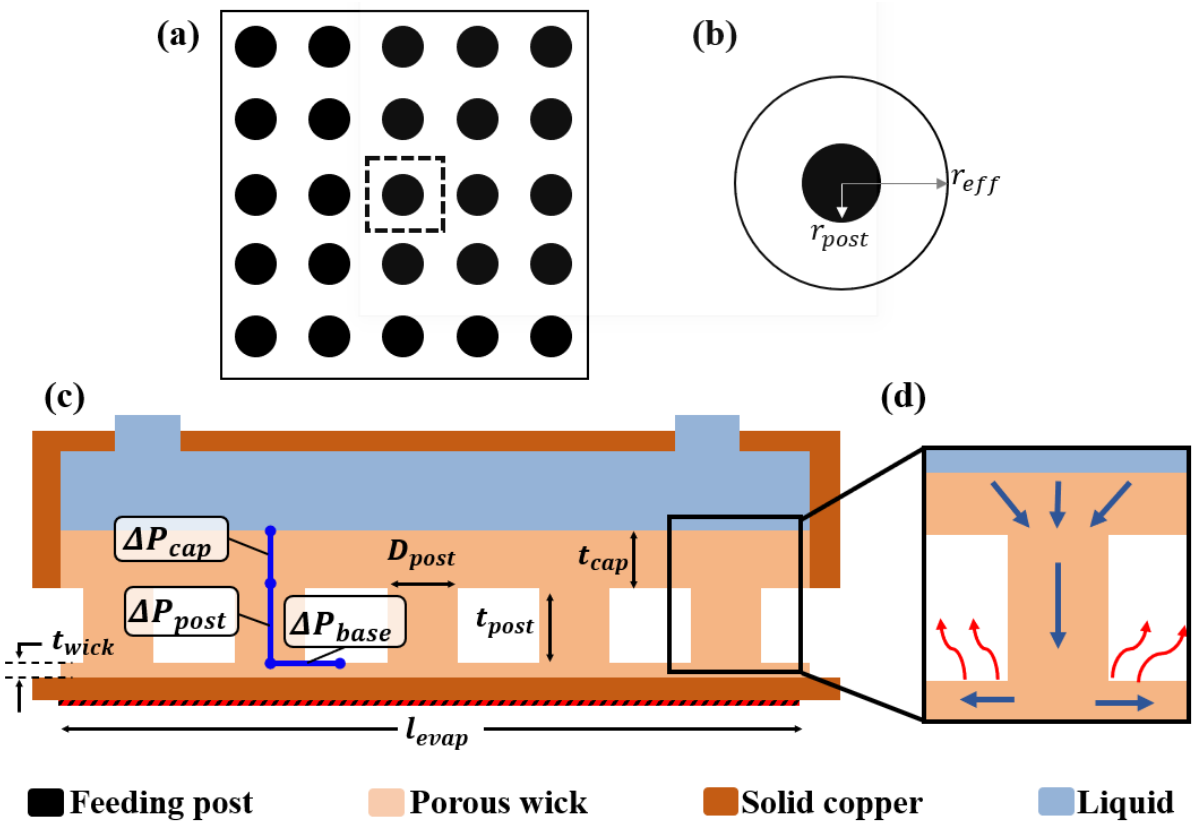

Figure 2.2. (a) Top-down view diagram of an evaporator base wick fed using a 5 × 5 array of feeding posts (filled circles), with an effective unit cell indicated by the black dashed line. (b) Radial approximation of the cell. (c) Cross-sectional schematic showing the location of the different pressure drop components and key geometric parameters. (d) Side view of radial approximation, with indication of the liquid pathway (blue lines), and location where phase change is occurring (red lines).

As a conservative assumption, the pressure drop through the cap layer is assumed to be confined to only the post area, ignoring any two-dimensional flow effects. A known relation for the permeability K is taken for sintered particle wicks [52]:

$$K = \frac{D_{part}^3 \phi^2}{450(1-\phi)^2} \tag{5}$$

where D_{part} is the particle diameter and ϕ is the porosity.

The expression for the pressure drop in the base wick is obtained from the one-dimensional momentum equation for radial flow in porous media

$$\frac{1}{\phi^2}\left(u_l\frac{\partial u_l}{\partial r}\right) = -\frac{1}{\rho_l}\frac{\partial P}{\partial r} - \frac{\nu_l u_l}{K} + \frac{\nu_l}{\phi}\left[\frac{1}{r}\frac{\partial}{\partial r}\left(r\frac{\partial u_l}{\partial r}\right) - \frac{u_l}{r^2}\right] \tag{6}$$

where the liquid flow velocity in the radial direction u_l through any wick with thickness t is defined as

$$u_l(r) = \frac{\dot{m}_{base}}{\rho_l(2\pi r t_{wick})}, \tag{7}$$

where $\dot{m}_{base}$ is the liquid mass flow rate, flowing radially outward from $r = 0$ to $r = r_{eff}$. The liquid mass flow rate increases from the center of the feeding post as it is uniformly fed and decreases due to evaporation outside the post radius. The mass flow rate ranges from a maximum value of $\dot{m}_{post}$ at the post radius ($r = r_{post}$) to a complete vaporization ($\dot{m}_{base} = 0$) at $r = r_{eff}$ as per [27]

$$\dot{m}_{base}(r) = \begin{cases} \dot{m}_{post}\left[\dfrac{r^2}{r_{post}^2}\right], & 0 \le r \le r_{post} \\ \dot{m}_{post}\left[\dfrac{r_{eff}^2 - r^2}{r_{eff}^2 - r_{post}^2}\right], & r_{post} \le r \le r_{eff} \end{cases} \tag{8}$$

Equation 6 is integrated from 0 to r_{eff} assuming that capillary-fed boiling occurs uniformly over the areas of the base wick not covered by posts, from the post radius to the effective post radius, resulting in a reduction of mass flowrate as specified in Equation 8. The pressure drop at the wick base is calculated to be

$$\begin{aligned} \Delta P_{l,base} = &\left(\frac{\rho_l c_1^2}{\phi^2} + \frac{\mu_l c_1}{K}\right)\frac{r_{post}^2}{2} \\ &+ \frac{\mu_l c_2}{K_{eff}}\left(ln\left(\frac{r_{eff}}{r_{post}}\right) - \frac{r_{eff}^2 - r_{post}^2}{2r_{eff}^2}\right) \\ &+ \frac{\rho_l c_2^2}{\phi_{eff}^2}\left(\frac{1}{r_{eff}^2} - \frac{1}{2r_{post}^2} - \frac{r_{post}^2}{2r_{eff}^4}\right) \end{aligned} \tag{9}$$

where

$$c_1 = \frac{\dot{m}_{post}}{2\pi\rho_l t_{wick} r_{post}^2} \qquad c_2 = \frac{\dot{m}_{post}}{2\pi\rho_l t_{wick}\left(1 - r_{post}^2/r_{eff}^2\right)} \tag{10}$$

The effective porosity (ϕ_{eff}) and effective permeability (K_{eff}) are explained in detail in Section 3.1.

2.2 Evaporator with Microtube Posts

The architecture with porous feeding posts described in the section above is modified by replacing the porous cap layer and posts with a solid copper manifold having copper microtubes that extend to the base wick. This architecture, shown in Figure 2.3 (c), removes not only the pressure drops inherent to the porous liquid pathway in the cap layer and posts, but relaxes the manufacturing limitations on the post diameter due to particle size, allowing a finer array for liquid feeding. Otherwise, this architecture concept shares the same key features including a fluid inlet and outlets, a compensation chamber, and feeding structures delivering liquid into the base.

For the prediction of the pressure drop and thereby maximum heat flux dissipation from the evaporator with microtube post, the same model assumptions from the porous post architecture are used; specifically, that capillary-fed boiling occurs uniformly over the area not covered by the posts, and that each post delivers liquid up to a certain effective radius within the base wick based on the post array size, calculated by equating the area of each feeding cell to that of a circular area with a radius r_{eff}.

$$\pi r_{eff}^2 = \frac{l_{evap}^2}{N_{posts}} \tag{11}$$

As a result, in the microtube evaporator concept, the only pressure drop working against the capillary pressure head is that in the base wick, and the same pressure drop expression in Equation 9 for the porous posts evaporator still applies. The maximum heat flux dissipation is calculated based on the two-phase pressure drop equaling the capillary pressure.

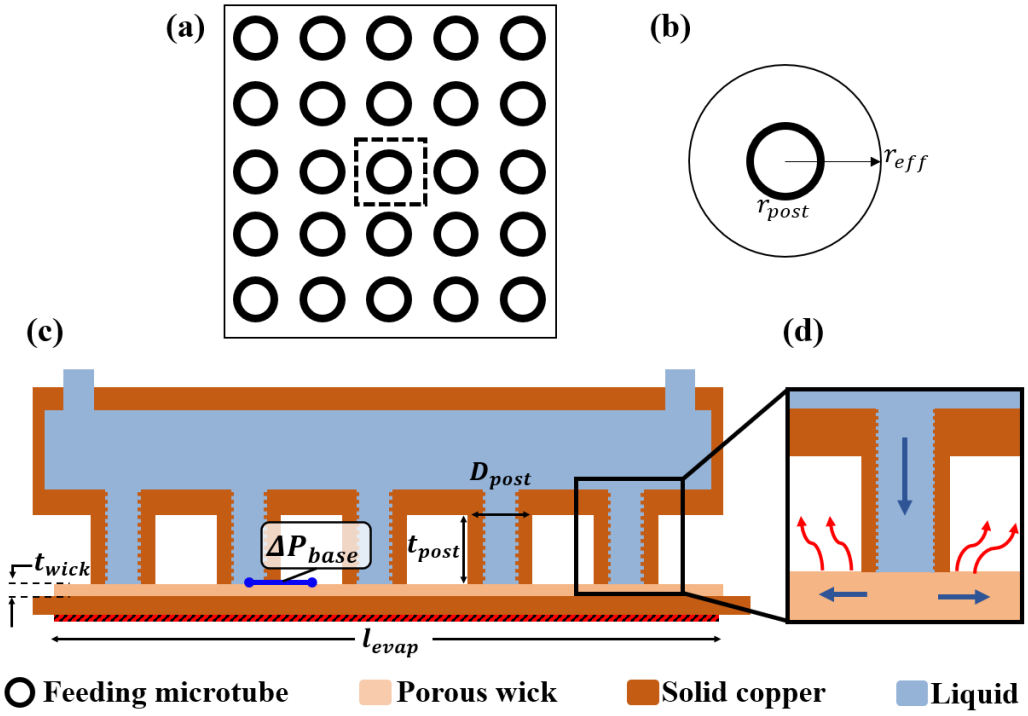

Figure 2.3. (a) Top-down view diagram of an evaporator base wick fed using a 5 × 5 array of feeding microtubes (unfilled circles), with an effective unit cell indicated by the black dashed line. (b) Radial approximation of the cell. (c) Cross-sectional schematic showing the location of the pressure drop component and key geometric parameters. (d) Side view of radial approximation, with indication of the liquid pathway (blue lines), and location where phase change is occurring (red lines).

3. RESULTS: MODEL-BASED EVAPORATOR DESIGN

The results chapter is divided into three subsections. The first section goes through a calibration required to obtain the effective porosity and permeability in the base wick due to account for the two-phase pressure drop. Then the parametric trends and the effect of different array sizes on the total power dissipation are explored. Lastly, the effects of different particle diameter size in the base wick are presented.

3.1 Porosity Fraction Calibration

The pressure drop through the wick base is derived assuming single-phase flow relations, and therefore requires correction to account for the vapor generated due to boiling in the wick. Following the approach presented in Ref. [27] to consider the reduction in available area for liquid to flow due to the vapor formation, an effective porosity (ϕ_{eff}) and effective permeability (K_{eff}) are used to calculate the pressure drop in the base (Equation 9). A parameter defined as the porosity fraction (PF) is included to modify the known wick porosity value, and thus, the permeability value.

$$\phi_{eff} = PF \cdot \phi \qquad K_{eff} = \frac{D_{part}^2 \phi_{eff}^3}{450\left(1-\phi_{eff}\right)^2} \tag{12}$$

The porosity fraction is taken as an empirical parameter that must be calibrated to experiments performed under capillary-fed boiling conditions in thin base wicks with a similar liquid-feeding arrangement. For this calibration purpose, data is available for capillary dry-out testing using a two-layer evaporator wick vapor chamber, obtained using the experimental setup and testing conditions as previously reported in Ref. [49]. The base wick characteristics input to the model and matching the experiments are listed in Table 3.1. Note that prior to testing, these wicks were submerged in a diluted piranha solution (sulfuric acid and hydrogen peroxide solution) to remove any surface contaminants, such that perfect surface wetting is assumed in the calculation of the wick capillary pressure. The fraction of area available for boiling listed in Table 3.1 corresponds to the relation between area available for boiling ant total evaporator area, calculated as

$$x_{evap} = \frac{A_{boil}}{A_{evap}} = \frac{1 - N_{post}\left(\pi D_{post}^2\right)}{l_{evap}^2} \tag{13}$$

where N_{post} corresponds to the total number of posts in an $n \times n$ array size.

Table 3.1. Wick characteristics from capillary dry-out testing used for calibration of the porosity fraction (PF).

Parameter	Value
t_{wick}	0.2 mm
t_{post}	0.5 mm
t_{cap}	0.8 mm
A_{evap}	1 cm^2
Array size ($n \times n$)	10 × 10
N_{posts}	100
D_{post}	0.5 mm
D_{part}	100 μm
x_{boil}	0.8

To perform the calibration, it is assumed that the total pressure drop has reached the maximum capillary pressure of the wick at the experimentally measured dry-out power. Considering a highly wetting fluid, the capillary pressure is defined as

$$P_{c,max} = \frac{2\sigma}{r_{pore}}, \tag{14}$$

where the pore radius is assumed to be 40% of the average particle radius [13]. For the system, the total pressure drop is

$$\Delta P_{total} = P_{c,max} = \Delta P_{cap} + \Delta P_{post} + \Delta P_{base} \tag{15}$$

Because the pressure drop in the cap layer and the posts are single-phase only, the only term affected by the porosity fraction is the pressure drop at the wick base (ΔP_{base}).

The PF value was adjusted until the total predicted pressure drop at the measured dry-out power (and corresponding mass flux) was equal to the maximum capillary pressure of the wick. A PF value of 0.172 was obtained from this calibration, which is then used throughout this work for all the two-phase pressure drop predictions within the base wick.

The fraction of area available for boiling was kept constant throughout this thesis to achieve a fixed temperature drop while varying the post diameter [48]. This resulted in a post diameter

decrease when looking at increasing array sizes. The post radius based on maintaining the boiling area constant for a squared $n \times n$ post array is calculated as

$$r_{post} = \sqrt{\left(1 - x_{evap}\right)\frac{r_{evap}^2}{n^2}} \tag{16}$$

where r_{evap} corresponds to the required equivalent radius to obtain the same evaporator area $A_{evap} = l_{evap}^2$.

3.2 Evaporator Design for Maximum Power Dissipation

Using the pressure drop model described in the previous sections, the effect of feeding feature (i.e., porous posts or microtubes) dimension, and thus array size, on maximum of heat flux dissipation were investigated for both evaporator concepts. Figure 3.1 plots the total pressure drop in the porous post design versus only the base wick component pressure drop as a function of the feeding post diameter for a single heat flux of 1 kW/cm^2. Note that because the microtube feeding post design comprising only the base wick pressure drop, this is effectively a comparison of the two different evaporator architectures. The parameters and variables kept constant for this study (unless otherwise noted) were the base wick thickness (t_{wick} = 0.2 mm) and particle average diameter (D_{part} = 100 μm), post height (t_{post} = 1 mm), and area available for boiling (x_{boil}). This allowed for the study to focus on the impact of microtube or post feeding size (and array size) required to achieve the required heat flux dissipation target of 1 kW/cm^2. Regardless of the dependence on post diameter, a first observation from Figure 3.1 is that the base wick pressure drop is the dominant main contributor to the total pressure drop, which is attributed to the thin wick and reduced area for liquid flow due to the porosity fraction. For the porous posts architecture, the liquid pressure drop due to the cap layer and the posts represents less than 10% of the total pressure drop.

Separately evaluating the trend with the post diameter, because the 1 cm^2 heat input area and the available boiling area not occupied by the posts is fixed constant, larger post diameters correspond to a smaller array size. Within smaller arrays at the same target heat load, each individual liquid feeding post must feed more liquid over a larger effective area. This in turn leads to a higher pressure drop in the base wick within increasing post diameter. Figure 3.1 also plots a horizontal line corresponding to the available capillary pressure, and the intersection of the

predicted pressure drop and this line determines the maximum allowable post diameter size to dissipate the specified heat load. It can be observed from Figure 3.1 that this minimum post diameter size required to be below the maximum allowable pressure drop line is <0.3 mm for the porous post design. By changing the evaporator structure design to the microtube manifold approach, the pressure drop is due to the base wick, but this provides only a very slight increase in the allowable post size for the reasons discussed above that the base wick dominated the pressure drop.

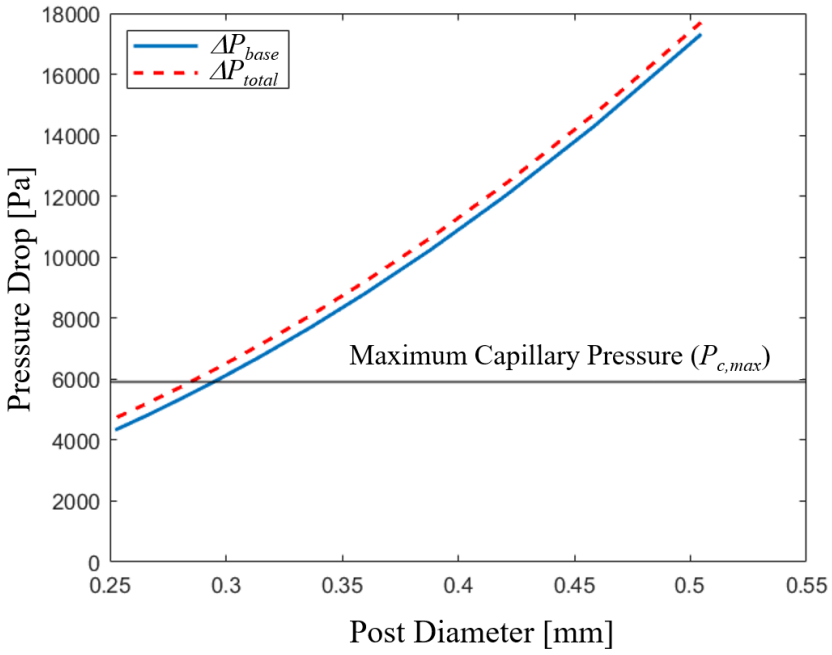

Figure 3.1. Comparison between the total pressure drop and the base pressure drop across different post diameters for a heat flux dissipation of 1kW/cm^2. The boiling area was kept the same for all the different post diameters at a value of x_{boil} = 0.8.

A study was performed to look at the maximum power dissipation capability for each of the evaporator architectures for $n \times n$ array sizes, and thus different post diameters as per Equation 16. Figure 3.2 presents a comparison of the maximum power dissipation for both evaporator architectures (porous and microtubing feeding into the wick).

In order to reach the dissipation target of 1 kW/cm^2, regardless of the evaporator architecture, the model predicts that a minimum array size of at least 18 × 18 feeding posts

distributed over the 1 cm^2 area is required to avoid dry-out (Figure 3.2). This represents post diameter of 0.28 mm. This post diameter can be manufactured for the microtubes architecture using various micromachining technologies but represents a significant manufacturing challenge for the porous post architecture. For the post integrity purposes, at least 3 particle diameters should be across the post diameter when working with sintered powder. From Figure 3.2, at this limit of a post diameter of 0.3 mm (corresponding to an array size of 16 × 16 posts) the pressure drop model predicts that the maximum power dissipation for the porous post evaporator architecture is ~800 W. One alternative option is for the porous post design to use smaller particles to form the evaporators; however, as will be further demonstrated in the coming Section 3.3., this comes at the cost of higher pressure drops in the base wick that ultimately limits the minimum particle close to this same value.

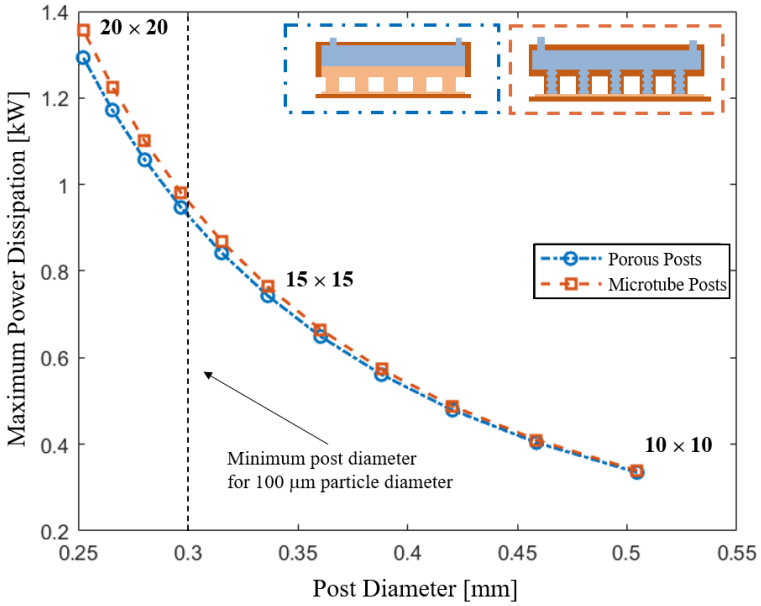

Figure 3.2. Maximum power dissipation for different post diameters and $n \times n$ array sizes (comparison between the porous post and microtube post architectures).

From the model predictions, an array of 18 × 18 microtubes over a 1 cm^2 area, each with a post diameter of 0.28 mm, is viable for dissipating the desired heat flux of 1 kW/cm^2. It was decided that an evaporator design having 20 × 20 liquid feeding microtubes (corresponding to a post diameter of 0.25 mm), which pushed the manufacturing capabilities to their limit, provides

some margin of confidence that this heat flux could be dissipated. Hence, these dimensions are the ones used for the detailed manifold design presented in the next chapter.

Even though the solid-walled microtubes provide a manufacturable alternative compared to the porous posts for enable finer arrays, various other potential liquid feeding configurations were considered during this work. In the architectures having cylindrical vertical feeding posts, to increase the area available for boiling in the evaporator, a trade-off must occur by making the feeding post smaller. One noteworthy alternative wick architecture was considered that attempted to decouple the available boiling area from the liquid feeding structure diameter, by adding boiling area to the feeding structures themselves, is presented and evaluated in Appendix A. Even though this 'area-enhancement' architecture was not predicted to meet the current objective of enhancing the dry-out heat flux due to other constraints, the concept holds promise for future designs where the additional boiling area may reduce the thermal resistance.

For the reasons listed in Sections 2.1 and 2.2, such as the post diameter limitation and the need of denser arrays to reach higher heat fluxes, it is decided to move forward with the micro-tubing architecture as the evaporator concept to be manufactured.

3.3 Wick Particle Size Effect

Using the model for pressure drop in the wick base, the effect of wick particle diameter is studied for at the fixed target heat flux dissipation of 1 kW/cm^2. Figure 3.3 presents the effect of wick particle diameter in the wick base pressure drop and the maximum capillary pressure corresponding to that diameter. Both the pressure drop and maximum capillary pressure increase as the particle diameter decreases; however, this rate of increasing pressure drop differs due to the different functional dependence on the particle sizes in Equations 9 and 14, respectively. This leads to a crossover point in the curves at a minimum particle size below which the pressure drop exceeds the capillary pressure and the evaporator wick would dry out. As presented in Figure 3.3, the minimum allowable particle diameter is 75 μm.

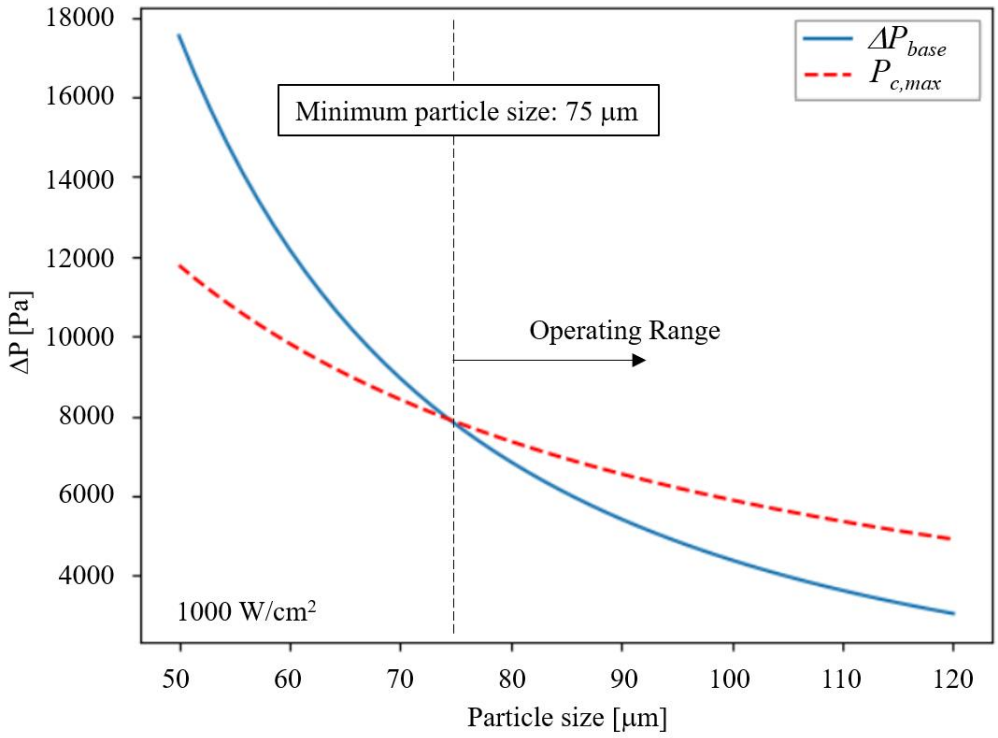

Figure 3.3. Effect of wick particle size on maximum allowable pressure drop.

Based on this parametric study, it is concluded that, for the manufacturing of the evaporator wick, the choice of base wick particle diameter must be above the specified minimum (75 μm); the default size of 100 μm used for all of the other above design evaluations is preferred because this was the same particle size used for experimental testing on which the porosity fraction parameter is calibrated.

3.4 Sensitivity to Porosity Fraction Parameter

The effect of the calibrated value of the porosity fraction (PF) on the predicted maximum power dissipation was studied. The uncertainty of the dryout power measurement presented in Ref [50] was used to obtain the PF range corresponding to the upper and lower uncertainty bounds of the experimentally tested dryout power. These lower and upper values are 0.169 and 0.175, respectively (i.e., ± 0.003 from the calibrated PF value). These values were used to calculate the maximum power dissipation prediction ranges for different post diameters. The resulting predictions are presented in Figure 3.4. Looking at the maximum power dissipation predictions for

the 20 × 20 liquid feeding microtubes (corresponding to a post diameter of 0.25 mm), the power ranges from 1.28 kW to 1.44 kW. Note that while this provides some estimate of the uncertainty due to this particular calibration, it is not meant to indicate the overall prediction accuracy accounting for the various other modeling assumptions described.

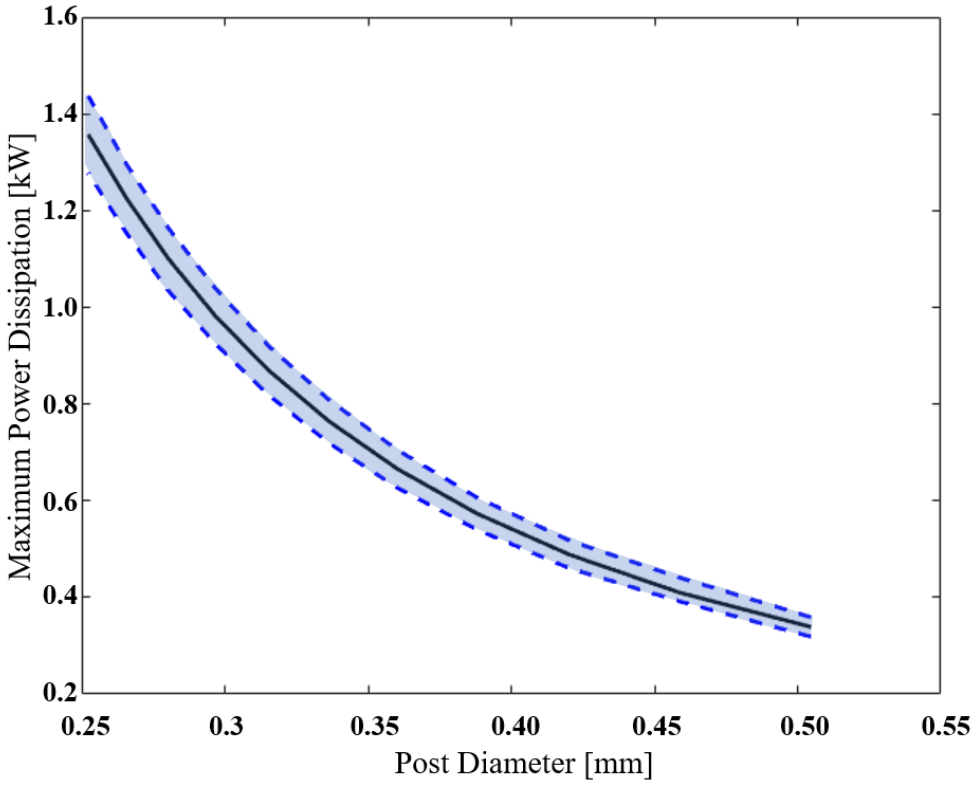

Figure 3.4. Porosity fraction effect on maximum power dissipation for the microtubes evaporator architecture. The solid line is the baseline prediction for PF = 0.172, whereas the lower and upper dashed lines correspond to the predictions for PF values of 0.169 and 0175, respectively.

4. PROTOTYPE EVAPORATOR TEST SECTION DESIGN, FABRICATION, AND ASSEMBLY

This section describes the design of a modular test section for characterizing the performance of prototype pump-assisted loop evaporators. The test section was designed to be compatible for integration into a flow loop located at the site of an industry collaborator, such that performance of various feeding and base wick configurations could be evaluated under applied testing conditions of interest. A physical prototype test section is fabricated and assembled with a microtube manifold and base wick parameters following the specifications identified from the model-based design in Chapter 3.

4.1 Flow Facility Description

The flow loop presented in Ref. [53] is available at the site of the industry collaborator for modification and adaptation to enable the testing of a PACL evaporator test section. The modified design of the flow loop, as developed in this this current work, is presented in Figure 4.1. The purpose of the loop is to provide liquid at a known subcooling temperature and flow rate to the compensation chamber of the evaporator, and also route any bypassed liquid and exhausted vapor for heat rejection to complete the cycle.

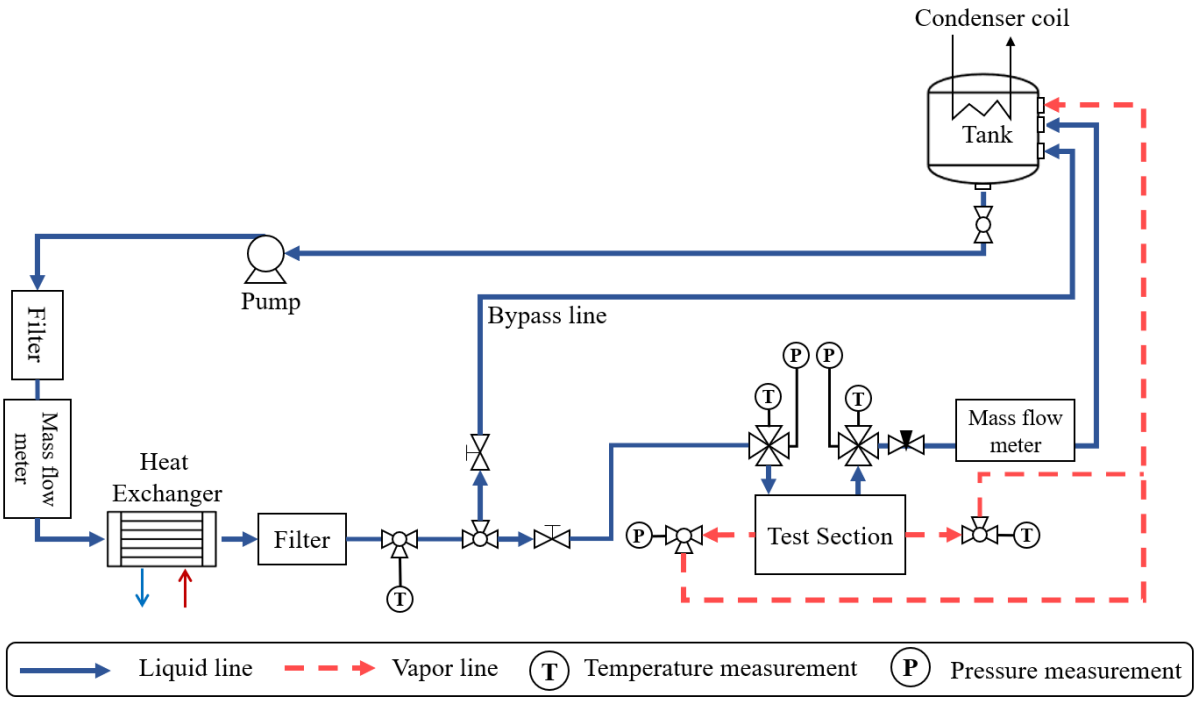

Figure 4.1. Flow loop diagram for the testing of the PACL evaporator test section.

The main components of the loop to be used to test the evaporator in the test section include a pump, a mass flow meter, an in-line heat exchanger for preheating, a set of filters, the test section, a reservoir with a condenser coil, and various valves and bypass lines for system control. A positive displacement pump is used to draw liquid from the reservoir. The flow provided by the pump is filtered and then measured by a Coriolis-effect mass flow meter that is controlled using a PID controller to maintain a constant flow rate. An in-line liquid-to-liquid heat exchanger pre-heats the liquid to a controlled subcooling temperature. A second filter is located at the outlet of the heat exchanger to prevent any particles flowing into the test section. Before the test section, a test section bypass line is located that connects directly with the reservoir. This bypass line allows for filling all the liquid lines prior to startup. Flow into and out of the test section is made through connections that allow for temperature and pressure measurements at the inlet and outlet of the liquid and vapor lines. An additional mass flow meter is located at the liquid test section outlet. The flow meter provides information regarding the fluid distribution between the exit lines (i.e., liquid vs. vapor). The vapor exiting the test section is condensed at the reservoir using a cooling coil located in the tank.

4.2 Test Section Design

A test section comprising the microtubes manifold evaporator architecture is designed to the dimensions and characteristics presented in Chapter 3. The overall test section (Figure 4.2) is composed of five assembled components: (1) a transparent cover, (2) a copper manifold, (3) a manifold support structure, (4) a copper base containing the sintered powder wick, and (5) a bottom carrier plate. A 1 cm^2 heater (not shown) is attached to the bottom side of the copper base and provides the power into to the evaporator. The parts are assembled and kept in place using a set of screws located around the circumferential periphery of PEEK elements (i.e., the manifold support structure and the bottom carrier plate). To secure sealing at the different faces, a combination of sealant, gaskets, O-rings, and face-sealing fittings is used.

This test section is designed to be modular and provides the flexibility of testing multiple base wick types and sizes (within certain limits) as well as insertion of different copper manifold to explore multiple feeding array configurations. Each of the individual components are described in the following subsections. All the mechanical drawings for the test section manufacturing are available in APPENDIX B.

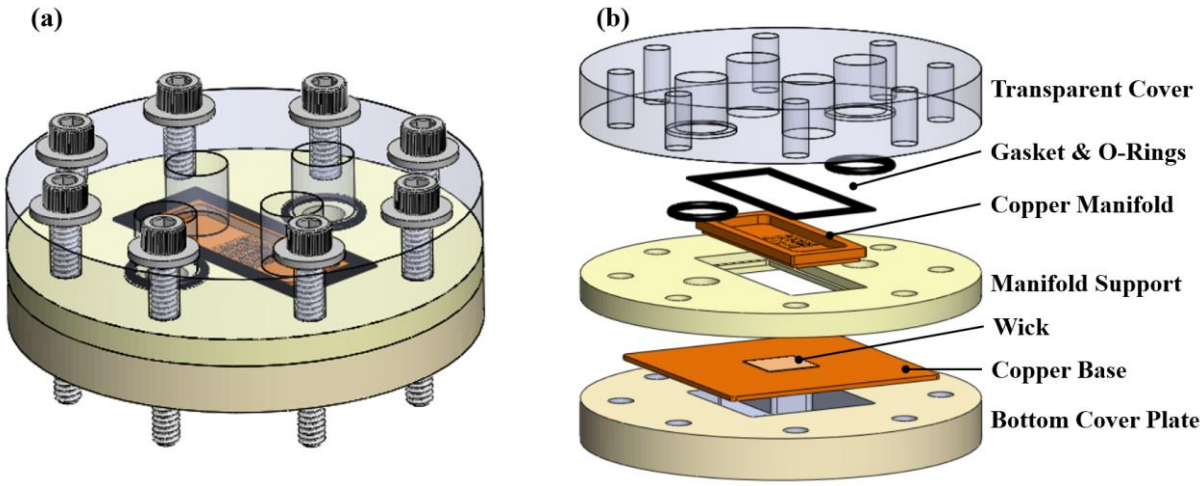

Figure 4.2. (a) An assembled view of the CAD model of the test section, including the screws used to keep the part together. (b) Exploded view of the test section (excluding the screws) with the main components indicated.

4.2.1 Transparent Cover

The transparent cover is machined from acrylic and is the upper most part of the assembly. It provides a physical barrier for liquid to be contained in the compensation chamber above the manifold, as well as an exit route for the vapor generated in the evaporator. The cover has two pairs of threaded ports for fitting attachment. The first pair of ports is used to deliver a route for liquid from the inlet to the outlet, while the second pair is used to extract vapor (i.e., both serve as outlets). The fluid to be delivered or extracted from each of the holes is identified by the presence or lack of circular grooves on the bottom side, for the vapor or liquid lines, respectively. These grooves are filled with an O-ring, as shown in (Figure 4.3 (c)), for vapor sealing between the manifold support structure and the transparent cover.

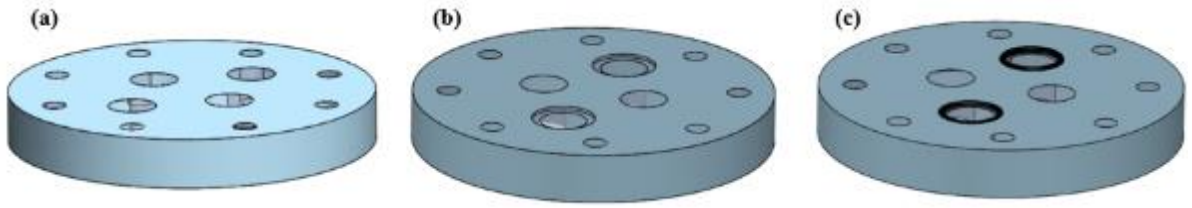

Figure 4.3. (a) Top view of the cover CAD model. (b) Bottom view of the cover CAD model, without O-rings. (c) Bottom view of the cover CAD model, including O-ring placement in the grooves.

4.2.2 Manifold

Based on the post diameter and array size analysis presented in Section 3.2, a manifold was designed to provide liquid feeding into the wick through microtubes. The feeding microtubes are distributed over an area of 12 × 12 mm^2 in the center of the manifold. This area populated with tubes is larger than the 10 × 10 mm^2 heater below to provide a 1-mm wide buffer that can accommodate any misalignment issues with the heater. In sum, a total of 572 tubes in the manifold corresponding to an array of 24 × 24 tubes minus the four corner tubes removed to accommodate the wick geometry.

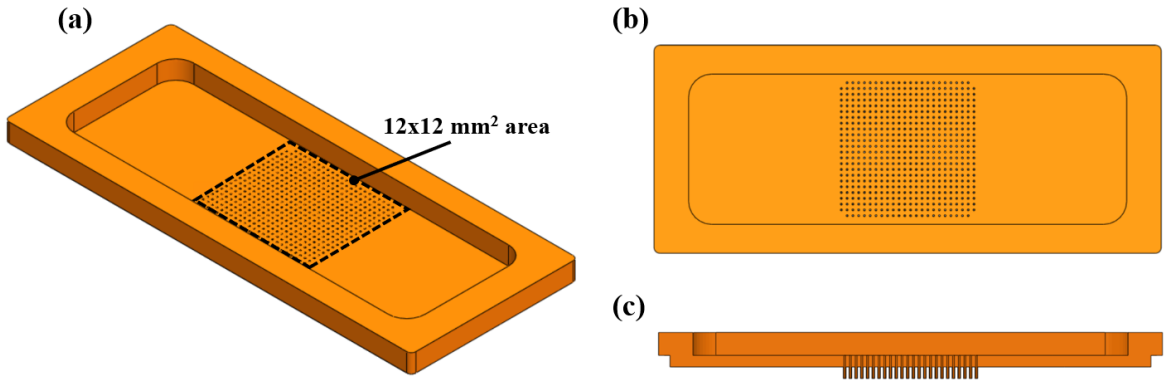

Figure 4.4. (a) Isometric view of the copper manifold CAD model. (b) Top view of the copper manifold CAD model. (c) Lateral cross-section of the copper manifold CAD model.

The manifold is manufactured by Sunlight-Tech Inc, by CNC micromachining. The microtubes have an outer diameter (OD) of 0.25 with a tube wall thickness (t_{tube}) of 50 μm, and a height (h_{post}) of 1 mm, measured from the base wick to the bottom face of the manifold. The tubes are spaced 0.5 mm from center to center. Figure 4.5 indicates the corresponding location to the dimensions.

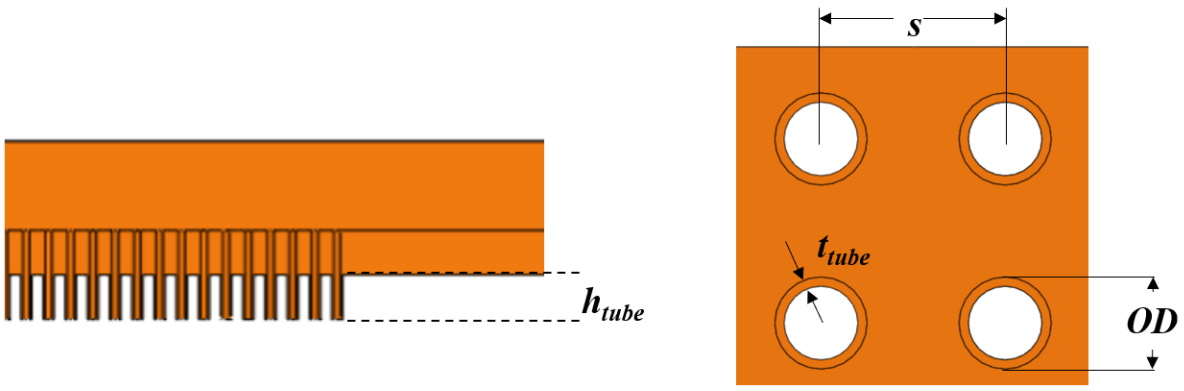

Figure 4.5. Manifold tubing dimensions.

To assemble the manifold into the manifold support structure below, there is a step along the entire outer perimeter on the bottom side of the manifold that seats into the upper recess of the

support structure. This step is sealed into the support structure using RTV sealant by applying a thin layer at the interface prior to its assembly. This type of assembly allows for the possibility of modifying the tube array characteristics (i.e., density, dimensions, etc.) without impacting any other assembly parts, simply by seating and sealing a new manifold into the support structure.

4.2.3 Manifold Support Structure

The manifold support structure is CNC machined from PEEK by Sunlight-Tech Inc. The main function of the support structure is to keep the key components of the assembly (i.e., the manifold and the copper base) aligned and in place; it also serves to form the vapor outflow path between the manifold and copper base. The upper recess (Figure 4.6 (a)) allows the copper manifold to seat in place from the top. A translucent RTV sealant (RTV118 translucent) is used to seal the part in place. Additionally, a thin silicone sheet is placed between the support structure and the cover, spanning across the manifold-PEEK interface; the silicone sheet is compressed with the cover providing sealing once the assembly is complete. On the bottom side, a squared recess is located to place the copper base and align the sintered copper wick with the feeding posts.

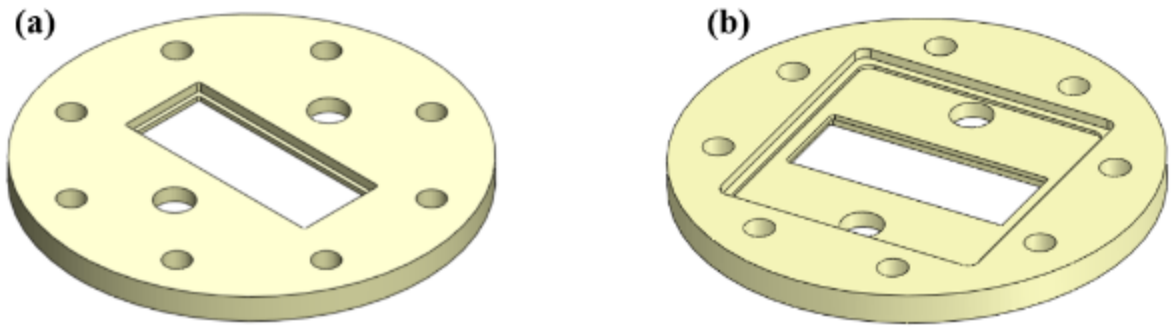

Figure 4.6. (a) Top view of the CAD model for the manifold support part. The centered rectangular recess is designed to fit the copper manifold. (b) Bottom view of the CAD model for the manifold support part. The top and bottom recess are designed to fit the copper manifold and base, aligning the wick area with the manifold microtubes.

Further detail on the bottom recess of the manifold support, is presented in Figure 4.7. This recess is designed so that the first point of contact between the manifold and the copper base occurs between the open, bottom ends of the copper microtubes and the top surface of the wick. This is

critical to ensure that there is no gap at this interface because of machining tolerances, which would cause leaking of liquid directly into the vapor outflow and compromise the functionality of the evaporator. A small step is also included around the perimeter of the bottom side recesses in the manifold support structure, pointed out in Figure 4.7. The resulting gap between the support structure and the copper base is filled with RTV sealant by applying it to the base edge prior to its assembly to the support structure. Although the baseline wick made for this test section has a 0.2 mm wick thickness, the design of the support structure allows for wick thicknesses up to 0.6 mm to be tested.

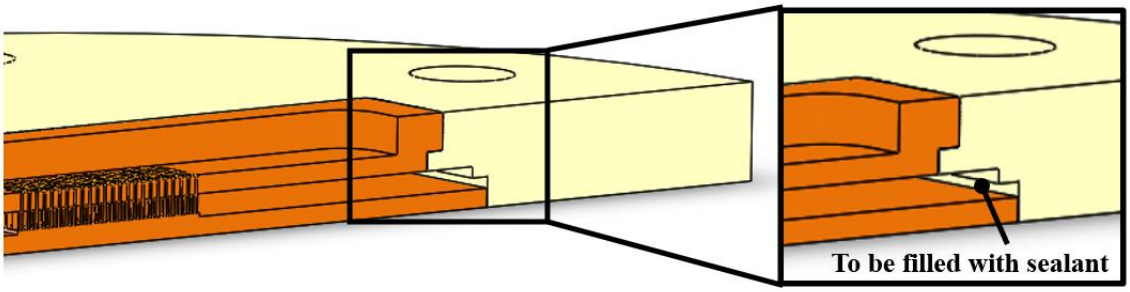

Figure 4.7. Assembly between the manifold, the manifold support, and the base, showing the gap that needs to be filled with sealant to prevent any leaks during the assembly.

4.2.4 Copper Base

The copper base consists of a square, 1 mm-thick, copper plate with the copper particle wick sintered at the center (Figure 4.8 (a)). A centered area of 12 × 12 mm^2 and 0.2 mm thickness is located on top of the copper plate. Copper particles with a sieved particle diameter ranging from 74 to 104 μm (Figure 4.8 (b)) are sintered to the plate using a mold, resulting in the evaporator porous wick. Having an average in particle diameter of 89 μm, the wick falls within the allowable particle size for the base wick as identified by the model predictions presented in Figure 3.3. The 0.2 mm-thick wick is kept the same as that used for the porosity fraction calibration.

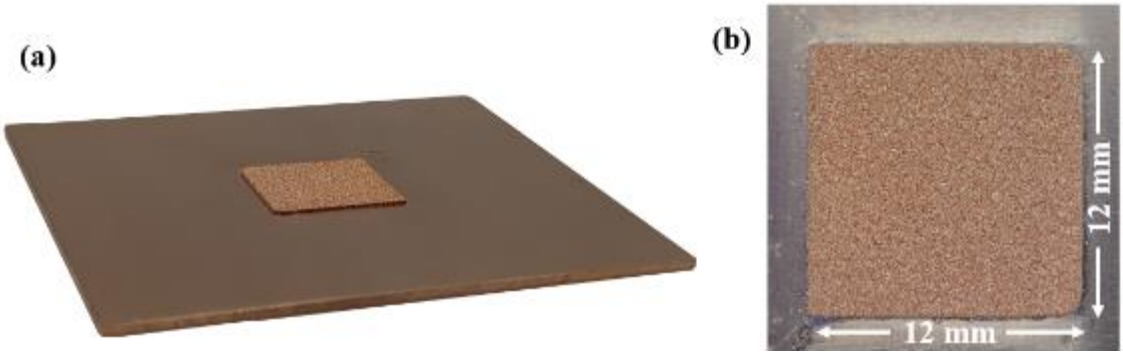

Figure 4.8. (a) Photograph of copper base with sintered copper wick at the center. (b) 89 μm average particle size wick

The entire manufacturing process for the base (i.e., the copper base machining and the wick sintering process) was performed by Celsia Inc. Due to manufacturing requirements during the sintering process, the corners of the wick include a 1.1 mm radius. As noted in Section 4.2.2 above, this required the removal of corner tubes in the manifold to prevent leaking of liquid past the wick and into the vapor outlet.

4.2.5 Bottom Carrier Plate

The bottom carrier plate is machined from PEEK by Celsia Inc. The main purpose of this part is to provide a protective layer between the copper base and surroundings. It has a centered window and a channel to facilitate the heater positioning and routing of wires.

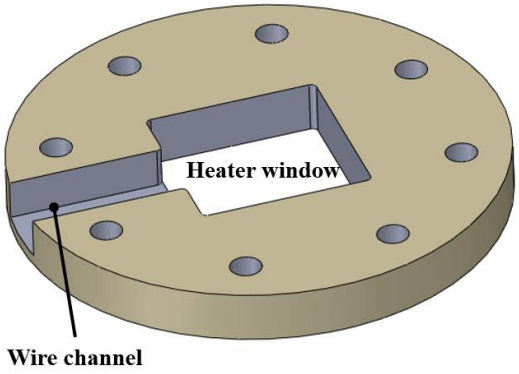

Figure 4.9. Bottom carrier plate and key features.

4.3 Test Section Assembly

The different evaporator parts were manufactured. The specification and design tolerances for a proper assembly are presented in the drawings shown in APPENDIX B. To connect the designed test section with the test facility without leaks, face-sealing fittings are used to connect the cover with the flow loop. Due to space restrictions, the fittings used to connect the liquid line are vertical, while the fittings used for the vapor outlet are 90° elbow-shaped as shown in Figure 4.10.

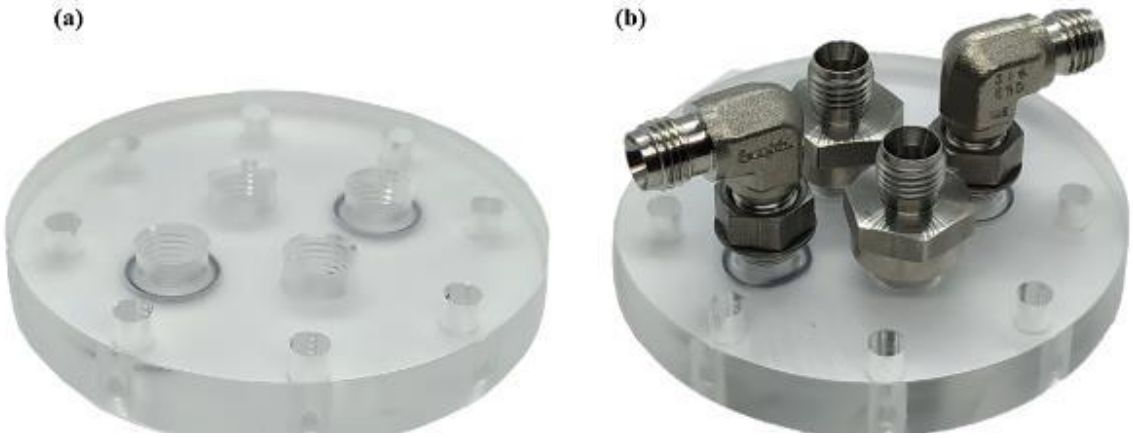

Figure 4.10. (a) Photograph of cover with the O-Rings in place. (b) Photograph of cover with the face-sealing fittings threaded on top.

Fittings are threaded to the cover to supply and remove both liquid and vapor. In addition to supply and extract fluids, fittings are also used to allow for measurements in the system while it is operating. To avoid any interference between the fittings, the measuring instruments, and the test section, the liquid enters and exits the test section vertically while the vapor outlets are in a lower plane. All the fittings used for this assembly are for ¼'' tubing. Additionally, all the threaded ports for temperature and pressure measurements are 1/8'' NPT female thread. Threaded thermal feedthroughs are used to insert T-type thermocouples for temperature measurements directly in the fluid and vapor lines. For the pressure measurements, OMEGA™ pressure transducers PX409-015G10V and PX409-030G10V are used for the liquid and vapor lines, respectively. The measurement points and flow direction for the liquid and vapor lines are presented in Figure 4.11.

The finalized assembly is presented in Figure 4.12 without the fittings to observe the components through the cover.

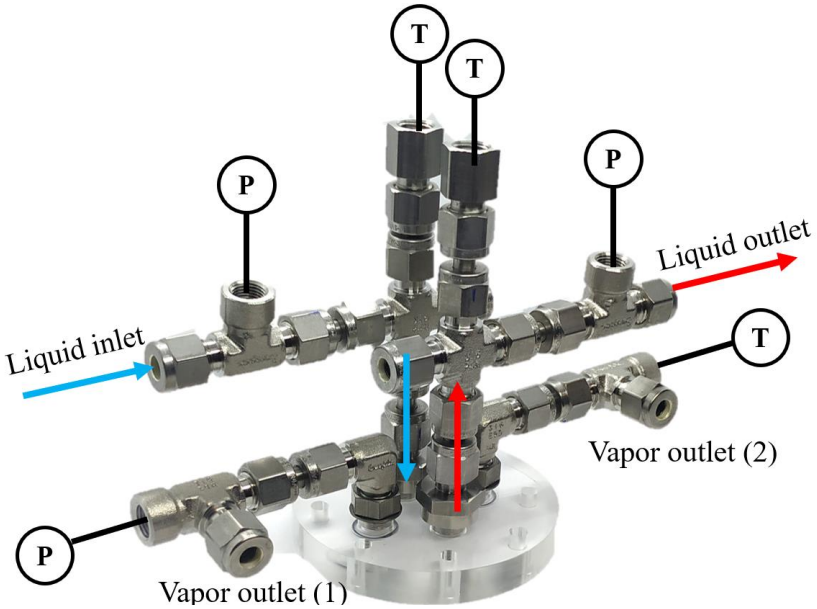

Figure 4.11. Liquid and vapor fittings attached to the cover and measurement points for liquid (in blue) and vapor (in red) lines.

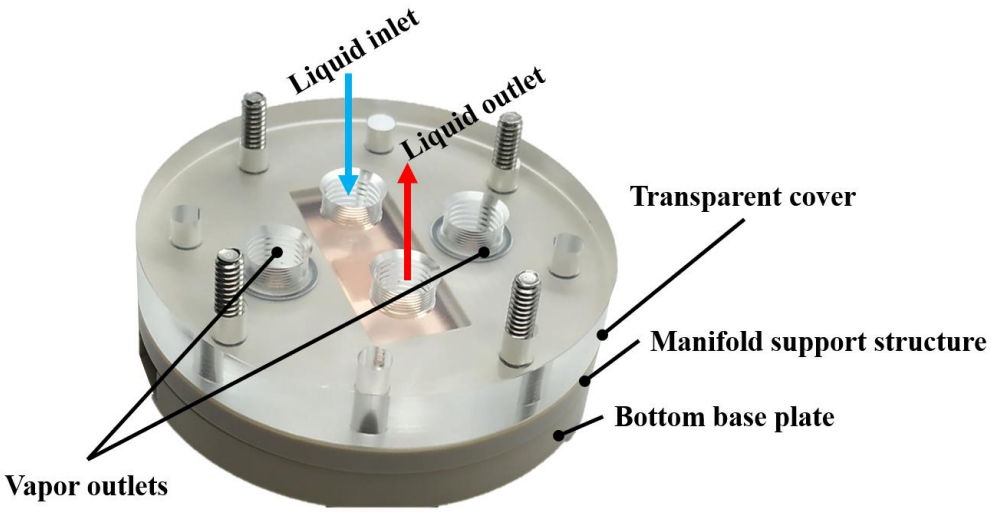

Figure 4.12. Photogram of the assembled test section for the evaporator of a PACL system without fitting connections.

5. CONCLUSIONS & FUTURE WORK

This chapter presents a summary of the key conclusions and findings on the design and manufacturing of and evaporator for a pump-assisted capillary system. Future research directions derived from this work are proposed.

5.1 Conclusions

In this thesis, a literature review identified that while multiple PACL systems have been built and tested, a gap exists for the design of a flat evaporator architecture that takes into consideration the operating parameters of the wick and the best way to feed liquid into the base to extend its dryout heat flux to ~1 kW/cm^2. To meet this need, the scope of the worked was focused on using an analytical model to predict the pressure drop prediction across the different elements of the evaporator. This included a calibration to experimental data to better predict the two-phase pressure drop occurring at the wick base due to capillary-fed boiling.

Two different evaporator architectures were compared for their use in a pump-assisted capillary loop system. While both architectures share the same general structure of a flat PACL evaporator, including a compensation chamber and thin base wick attached to the heater, the architectures differed in the method of feeding liquid from the chamber to the base wick. The first porous evaporator wick used porous sintered particle columns placed in an array to make the capillary liquid connection, similar to previous PACL evaporators in literature and in two-layer vapor chamber wick structures. The second architecture proposed an alternative that uses a copper manifold of microtubes. Both architectures had the same base structure, which was a sintered coper particle wick.

Using an analytical model for pressure drop calculation through porous media, different liquid feeding post array densities were modeled and their maximum heat flux dissipation calculated. The design objective was to provide a set of dimensions to be manufactured with the capability to dissipate heat fluxes of ~1 kW/cm^2. The analytical model also yielded a minimum particle size allowed in the base wick manufacturing to reach the dissipation objective.

To consider the effect of capillary-fed boiling in the base wick, an empirical correction was implemented in the single-phase pressure drop relation used to predict the pressure drop though

this wick layer, which represented the dominant contributor to pressure drop. Specifically, this correction took the form of a porosity fraction parameter to account for the area reduction due to boiling in the base wick. This parameter was calibrated using previous dry-out experimental data available from similar wick dimensions and top-down distributed feeding strategy. The model developed was used to parametrically evaluate the impact of feeding feature size, while keeping the available area for boiling and wick base layer thickness constant.

To reach high heat flux dissipations such as 1 kW/cm^2, the required size of the liquid feeding columns/tubes was identified to be ~0.25 mm or less. While this dimension violates some of the constraints for manufacturing the porous posts using the particle size predicted to be required for the base wick, the alternative microtube manifold architecture provides a feasible alternative to deliver liquid into the base in using a denser array of tubes.

The microtube manifold provides an additional advantage when working in a PACL system to enhance the maximum power dissipation. To overcome the dryout power limit defined by the base wick's maximum capillary pressure, the compensation chamber can be pressurized using the upstream pump and the valve located at the evaporator outlet. By increasing the compensation chamber pressure, liquid can be forced to flow through the microtubes and onto the base wick. This will generate a partially flooded condition in the evaporator base, allowing the possibility to overcome the capillary driven dryout power.

A modular test section design was manufactured to test this novel manifold architecture for capillary-fed boiling in a PACL system. The modularity of the design allows different wick thicknesses and particle sizes (within a certain footprint and thickness), as well as different post array configurations to be tested, without impacting the other parts of the design (i.e., the cover, support structure and bottom carrier plate).

5.2 Future Work

Future work for this thesis includes testing of the designed evaporator architecture, benchmarking its performance against available cooling technologies, and the design and analysis of new evaporator architectures.

Recalling from the introductory chapter of this thesis, a qualitative comparison presenting the advantages of a PACL system against other single- and two-phase systems was presented and discussed (Table 1.1). The experimental testing of the evaporator designed and manufactured in

this work will provide data to perform a benchmark analysis against these alternative cooling technologies. This benchmarking will result in a quantitative comparison between cooling technologies so as to confirm or correct the hypothetical statements in the table.

As presented in this work, the top-feeding strategy of the wick using porous posts or microtubes has sizing limitations where – to further increase base feeding spots - the feature size must become smaller. To overcome the limitations presented in this thesis regarding feature size, different feeding strategies musts be taken into consideration. A concept developed and presented in APPENDIX A does not rely on vertical feeding features or boiling in a flat base wick; it proposes an architecture where boiling is occurring from the vertical walls of particle covered features. While the projected power dissipation of this concept is below the target heat flux for the scope of this work, its manufacturing and testing could provide valuable information about the operating characteristics of this type of novel architecture.

There is also an increasing interest in taking advantage of non-conventional manufacturing techniques, such as metal additive manufacturing [54], [55] and 3D printing [56] to fabricate concepts that would not be possible using traditional machining. The implementation of these available technologies adding to the modeling strategies for pressure drop across porous surfaces can produce a new evaporator design that takes advantage of the pumping power of a PACL, provides high heat flux dissipation, and is compact.

APPENDIX A. SURFACE AREA ENHANCEMENT EVAPORATOR

A.1. Surface Area Enhancement Concept

One of the main limitations with a conventional evaporator, as presented in the main sections of this work, is the trade-off between adding more feeding points to prevent dry-out and maintaining enough boiling area. This inevitably leads to very small feeding features that limits the manufacturing options.

A different evaporator architecture is presented as an alternative to traditional evaporators having uniform, flat base wicks. This evaporator architecture shares some characteristics with the concepts presented in this work, such as a flat evaporator structure and a compensation chamber. The liquid in the compensation chamber fully saturates a wick layer responsible for distributing the liquid across the 'enhancement features. Rather than having the boiling occurring in the wick base, the surface area enhancement evaporator refers to surface enhancement features (i.e., porous-coated vertical structures). With the addition of vertical porous coated features, the boiling lateral area can be increased within the same evaporator footprint. A diagram showing the key dimensions is presented in Figure A.1.

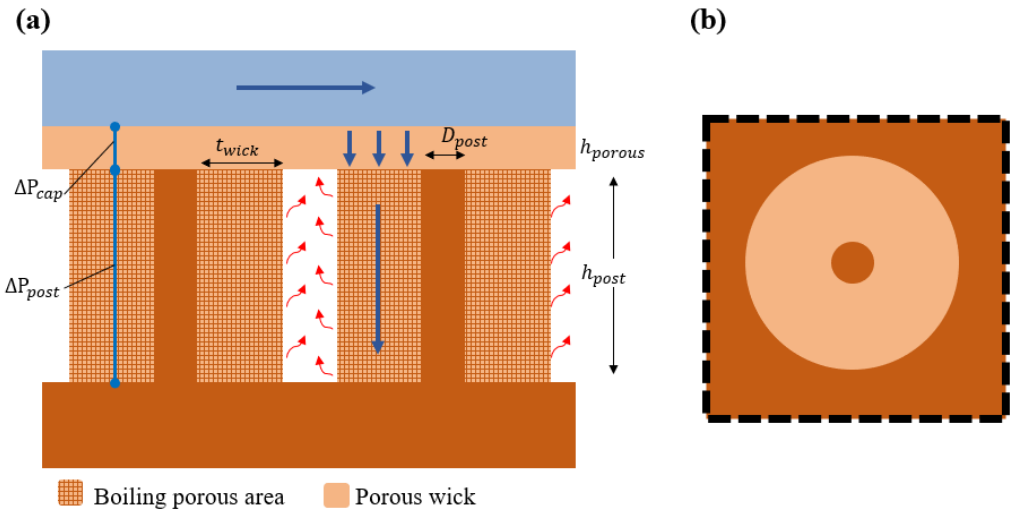

Figure A.1. (a) Schematic diagram for the area enhancement evaporator with a circular cross-section viewed from the top (b).

The area availability ratio (AAR) is defined as the relationship between the lateral area available for boiling and the evaporator footprint and it is only a function of the geometric parameters of the enhancement features (i.e., height and wick thickness). An AAR value of 1 represents that the vertical area available for boiling is the same as the evaporator horizontal footprint. For a porous post evaporator with a traditional base wick, the AAR could never be greater or equal than unity because of the need to add feeding posts into the wick removes available wick area that could be used for boiling. For the evaporators presented in the main sections of this work, the AAR is 0.8. The impact of different wick thicknesses and post heights for a circular cross-sectioned feature is presented in Figure A.2.

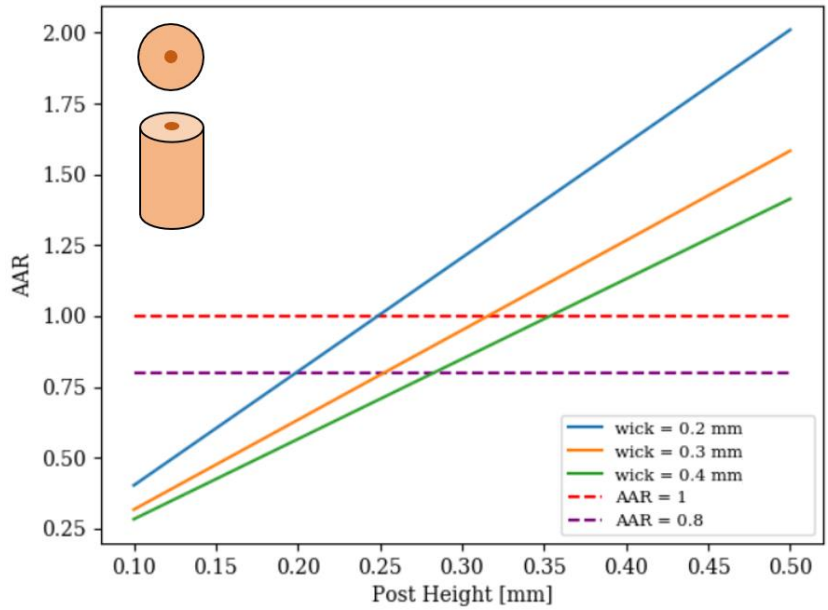

Figure A.2. Area availability ratio (AAR) for cylindrical-shaped posts, varying height, for different wick thicknesses. An AAR value of 0.8 is indicated as reference because it corresponds to the value used for evaporator architectures having flat base wicks presented in this work.

The surface area enhancement evaporator concept can achieve AAR values greater than unity, providing more boiling area than that originally available from the evaporator's footprint. Depending on the wick thickness, a post height of 0.24, 0.33, and 0.35 mm is required for a wick thickness of 0.2, 0.3, and 0.4 mm, respectively. For the same AAR, taller posts are required for thicker wicks. Since the evaporator footprint is limited, less features can be added within the same space when the feature is thicker overall.

A.2. Pressure Drop Models

Starting from the one-dimensional momentum equation in porous media

$$\frac{1}{\phi^2}\left(u_l \frac{\partial u_l}{\partial z}\right) = -\frac{1}{\rho_l}\frac{\partial P}{\partial z} - \frac{\nu_l u_l}{K} + \frac{\nu_l}{\phi}\left[\frac{\partial^2 u_l}{\partial z^2}\right] \quad \text{(A. 1)}$$

and defining the mass flowrate across the post as

$$\dot{m}_l(z) = \dot{m}_{post}\left[\frac{z}{h_{post}}\right] \quad \text{(A. 2)}$$

where the mass flowrate per post is obtained by dividing the evaporated mass flowrate (directly related to the power input and heat of vaporization) between the number of posts available in the design.

Assuming an axial flow velocity for a circular cross-section feature as

$$u_l(z) = \frac{\dot{m}_l}{\rho A} = \frac{\dot{m}_{post}}{\pi\rho[t_{wick}^2 + t_{wick}\cdot D_{post}]}\left[\frac{z}{h_{post}}\right] = B \cdot z \quad \text{(A. 3)}$$

where *B* is a constant that is only dependent on the feature size and geometry. Integrating Equation A.1 from 0 to h_{post}, the total pressure drop of the post is calculated to be

$$\Delta P_{post} = \frac{\rho_l}{2}\left[\frac{\nu_l B}{K_{eff}} + \frac{B^2}{\phi_{eff}^2}\right] h_{post}^2 \quad \text{(A. 4)}$$

Because boiling is occurring on the walls of the enhancement features, the effective porosity and permeability are used, as explained in Chapter 3.1. The same PF value of 0.172 is used for the two-phase pressure drop predictions on this section. However, it is recognized that the PF value was obtained from testing performed on an entirely different architecture, and so the pressure drop results here should only be used to understand trends until a proper calibration has been performed on a lateral boiling evaporator of this nature.

A.3. Heat Dissipation Predictions

The main goal of this architecture is to provide an increase in the boiling area compared to the traditional architectures. For this reason, an AAR target of 1 is used to fix the post height required (0.24 mm for a 0.2 mm wick thickness). With the post height fixed, at 550 W the pressure drop on the posts reaches the maximum allowable pressure drop, dictated by the wick's capillary

pressure. The 0.2 mm wick thickness was used as reference, because the porosity fraction parameter used to predict the two-phase pressure drop in the wick is calibrated using that thickness.

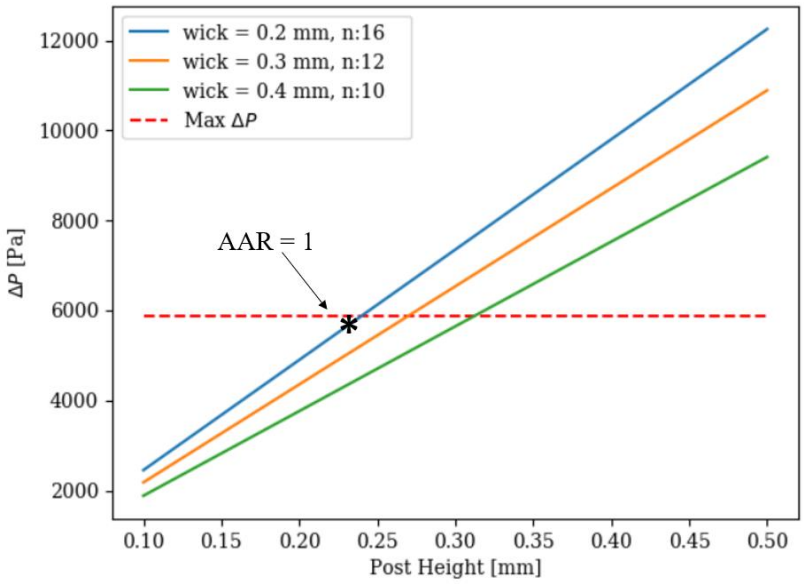

Figure A.3. Pressure drop predictions for a 550 W/cm^2 heat flux input. Three different wick thicknesses are presented, also indicating the maximum n x n array size in an evaporator footprint of 1 cm^2.

While the surface area enhancement evaporator provides a lower heat dissipation limit to that of a traditional base boiling concept, it does provide more boiling area and is therefore of interest as a technical that might reduce the thermal resistance. However, because the PF parameter used for the area enhancement evaporator was calibrated using experimental work with a different architecture wick, the maximum power dissipation prediction of 550 W would need to be corroborated experimentally, and the PF parameter updated accordingly.

A.4. Proposed Manufacturing Process

The proposed manufacturing process for the surface area enhancement evaporator consists of 5 steps (Figure A.4 (a.1 – e.1)). Starting from a solid copper block, the core features are machined. These features are then covered with sintered copper powder. The excess of copper powder is then removed to create space between features for boiling to occur and allow vapor to exit. A final sintering process takes place with the part placed up-side down. This last step provides

the cap layer that is in contact with the single-phase liquid in the compensation chamber. A similar process was successfully performed to generate the two-layer wick presented in [49]. A test section redesign, specifically for the PEEK support structure, would be required to support the surface area enhancement evaporator testing.

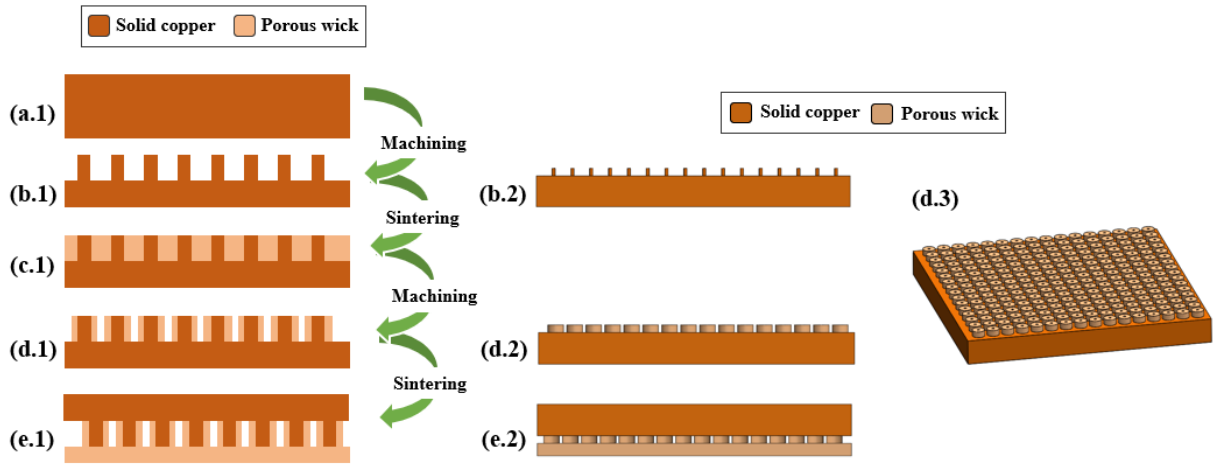

Figure A.4. (a.1 – e.1) Proposed manufacturing sequence for a surface area enhancement evaporator with a circular face. (b.2 – e.2) Lateral views for the 3D model at the second, fourth and last stage of the proposed manufacturing process. (d.3) Isometric 3D view for the third step in the manufacturing process proposal.

APPENDIX B. DESIGN DRAWINGS FOR EVAPORATOR TEST SECTION

B.1. Manifold Drawings

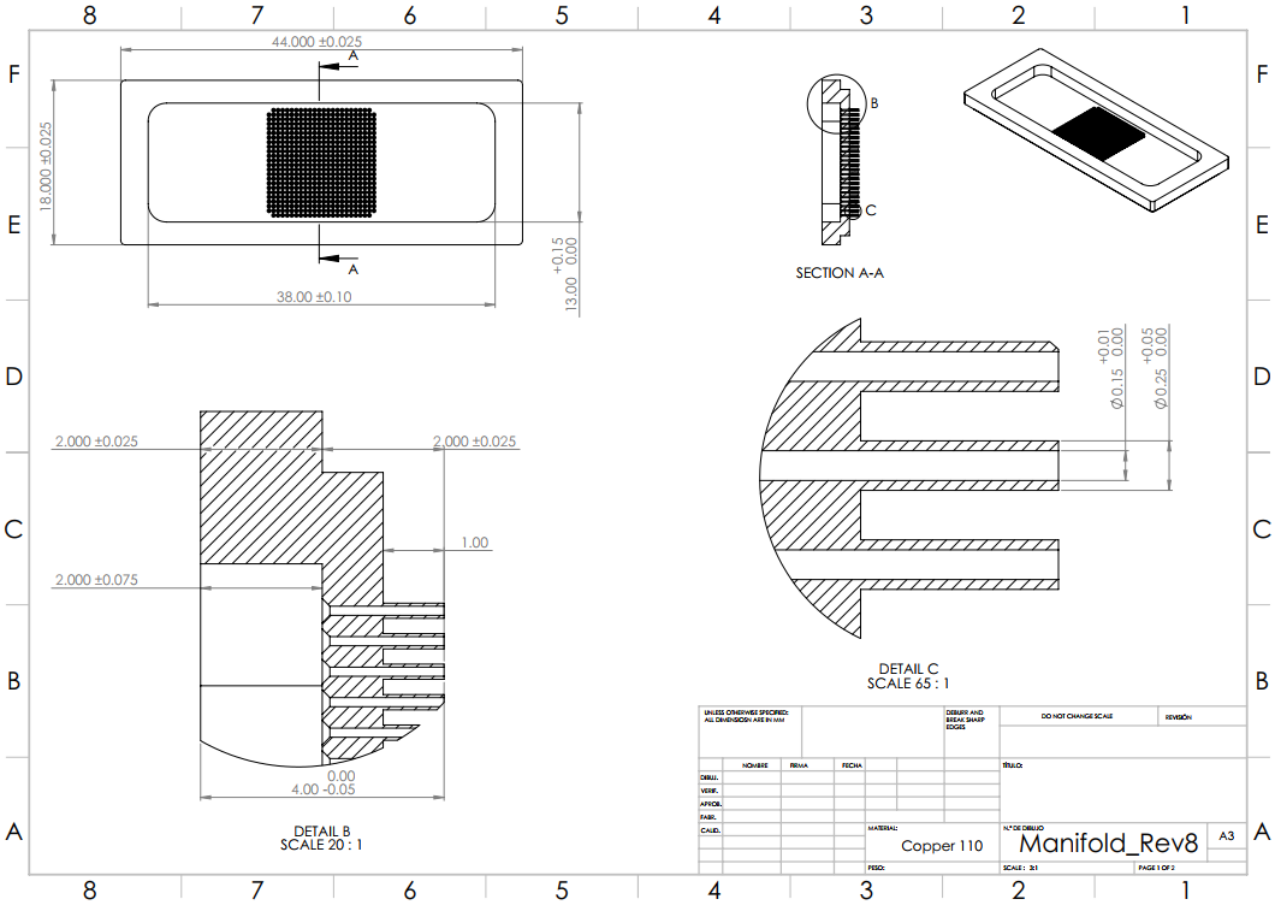

Figure B.1. Page 1/2 for the mechanical drawing of copper manifold.

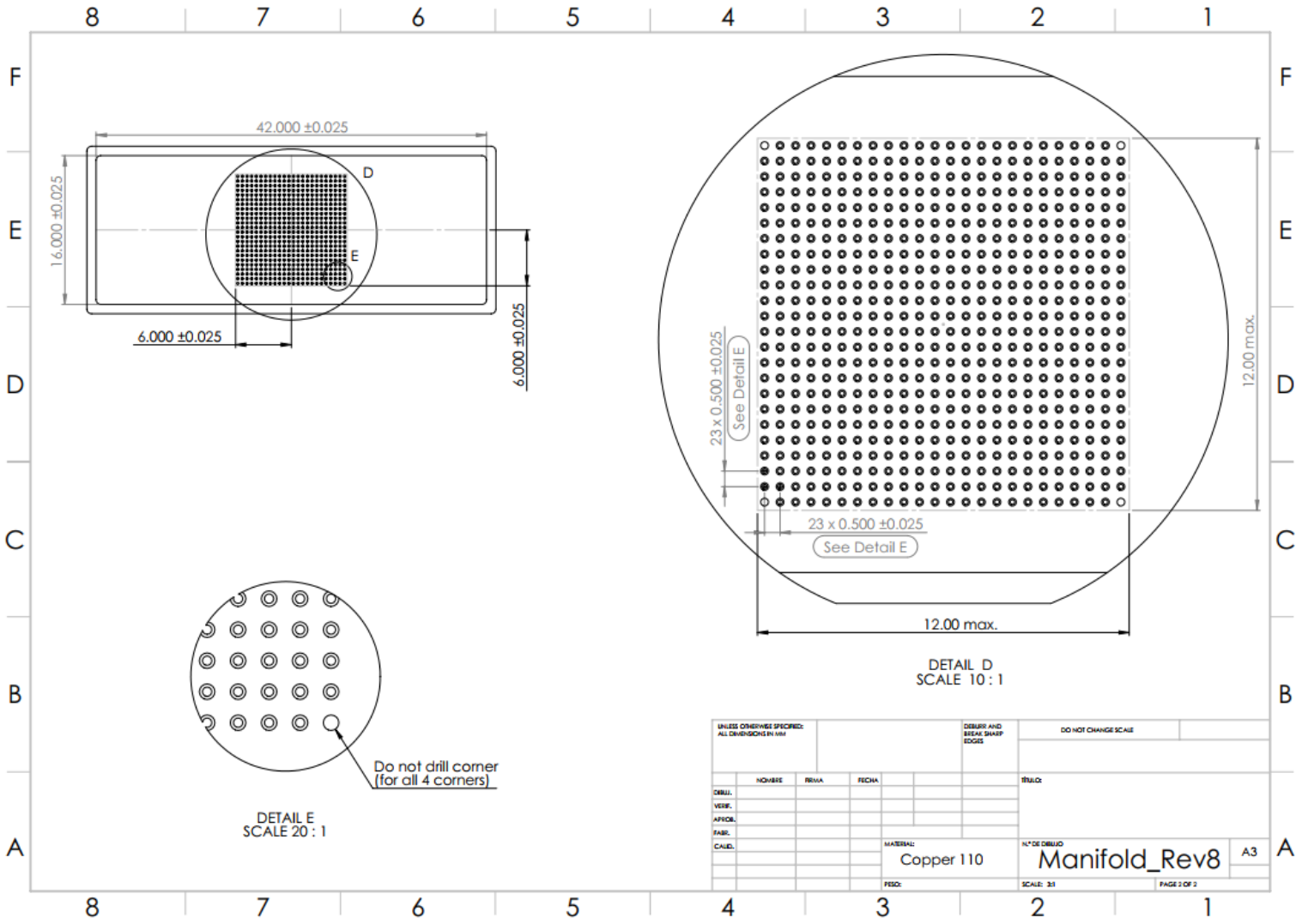

Figure B.2. Page 2/2 for the mechanical drawing of copper manifold.

B.2. Manifold Support Structure Drawings

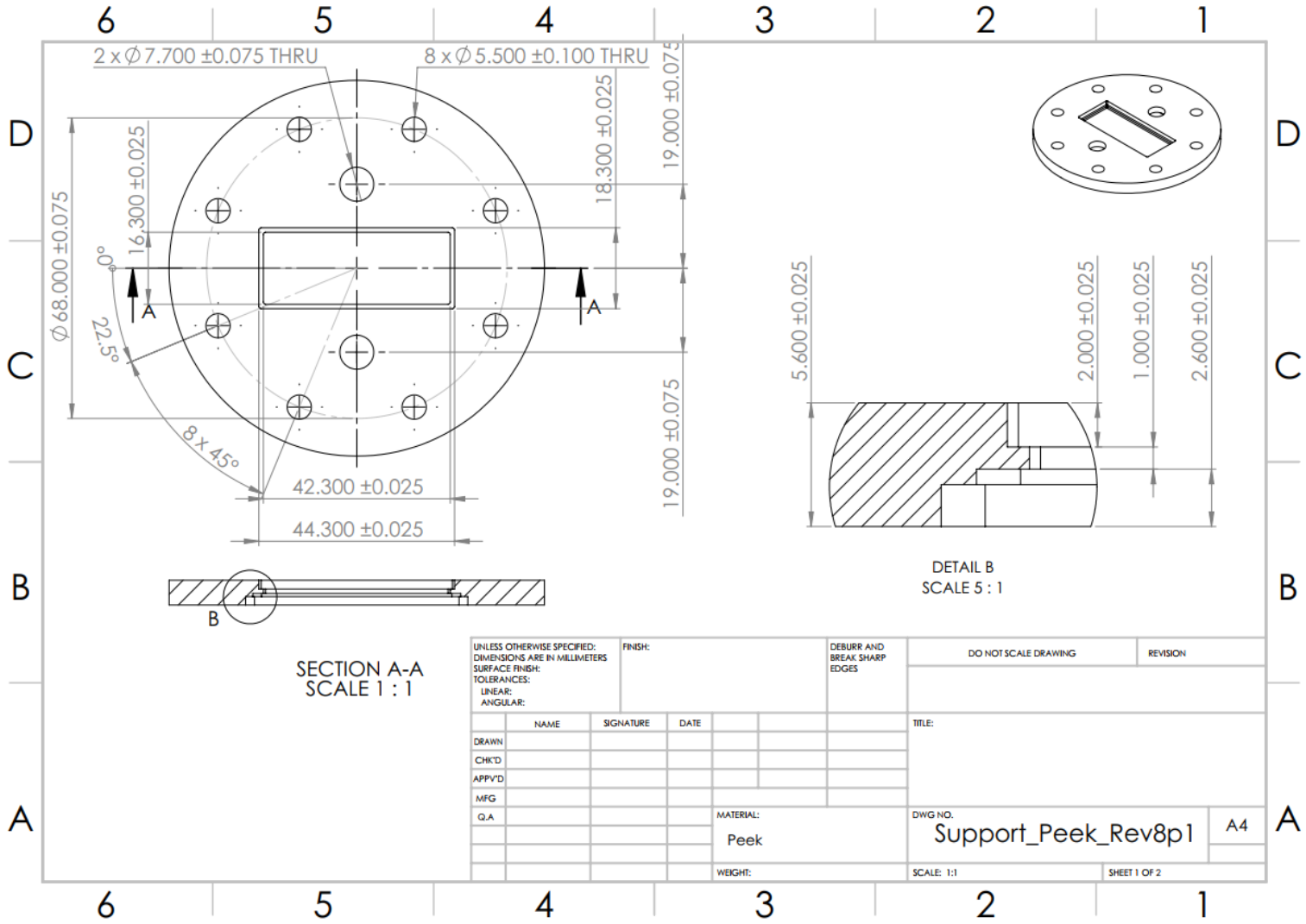

Figure B.3. Page 1/2 for mechanical drawing of PEEK support structure.

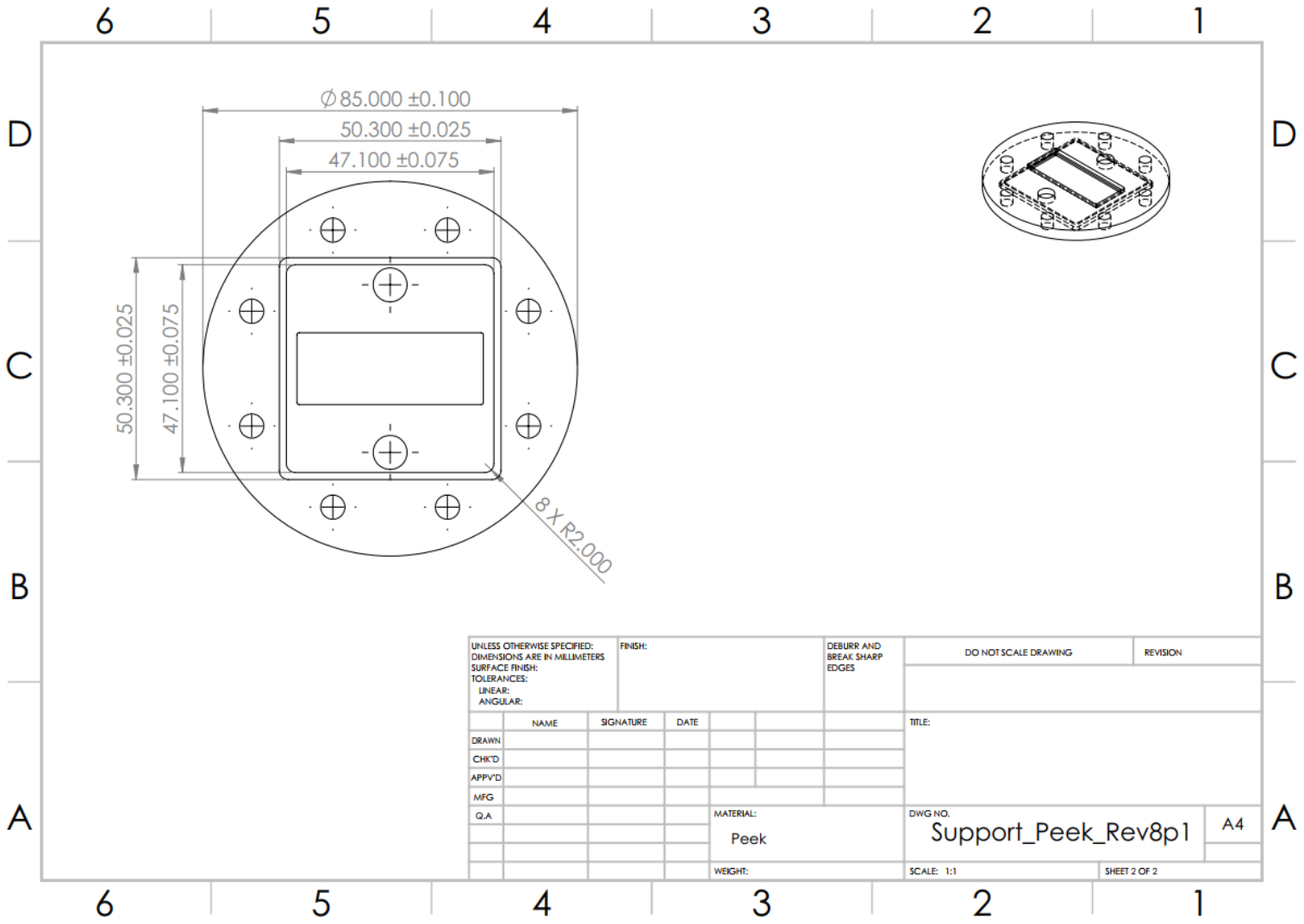

Figure B.4. Page 2/2 for mechanical drawing of PEEK support structure.

B.3. Cover Drawings

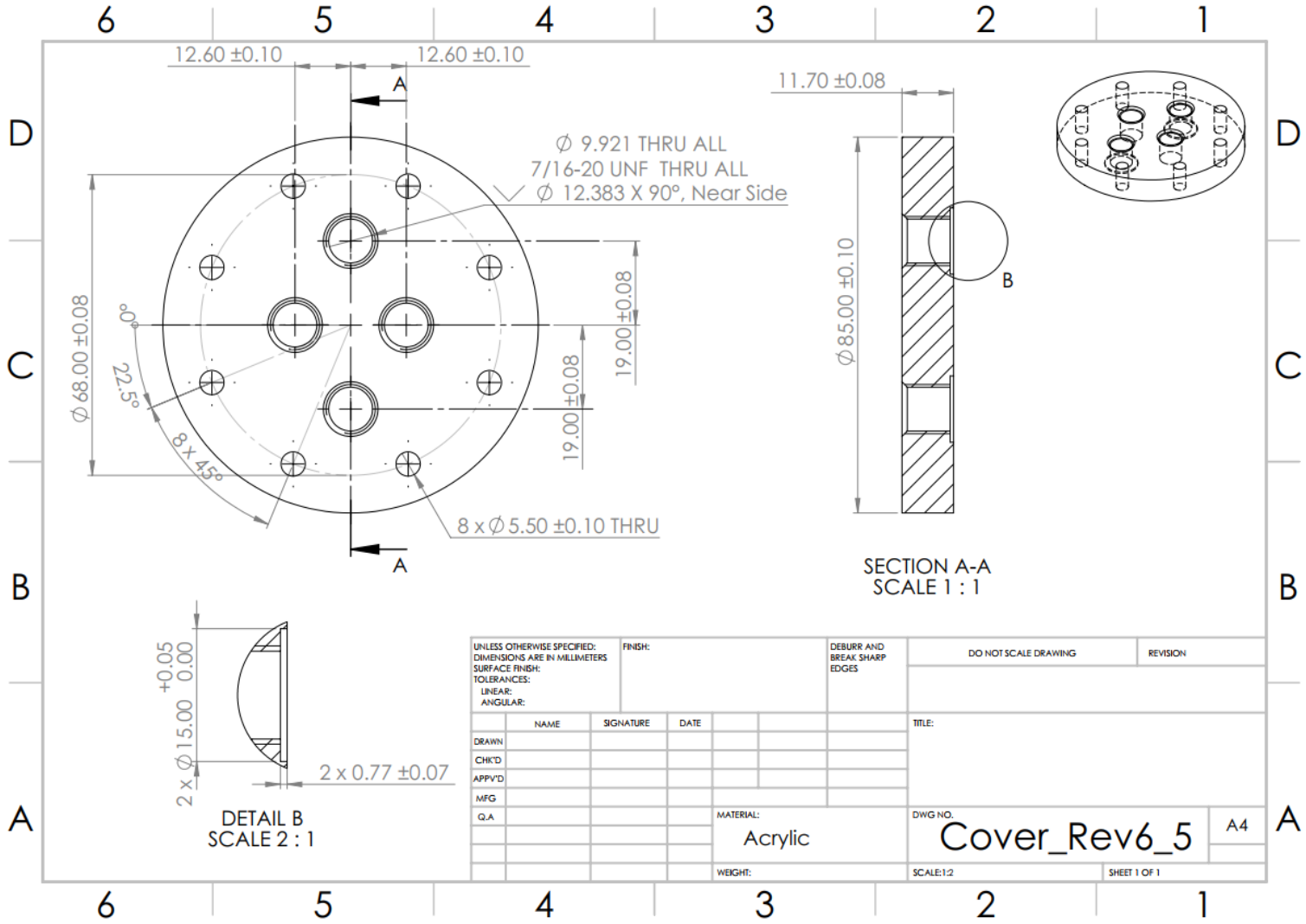

Figure B.5. Mechanical drawing of acrylic cover.

B.4. Copper Base and Wick Drawings

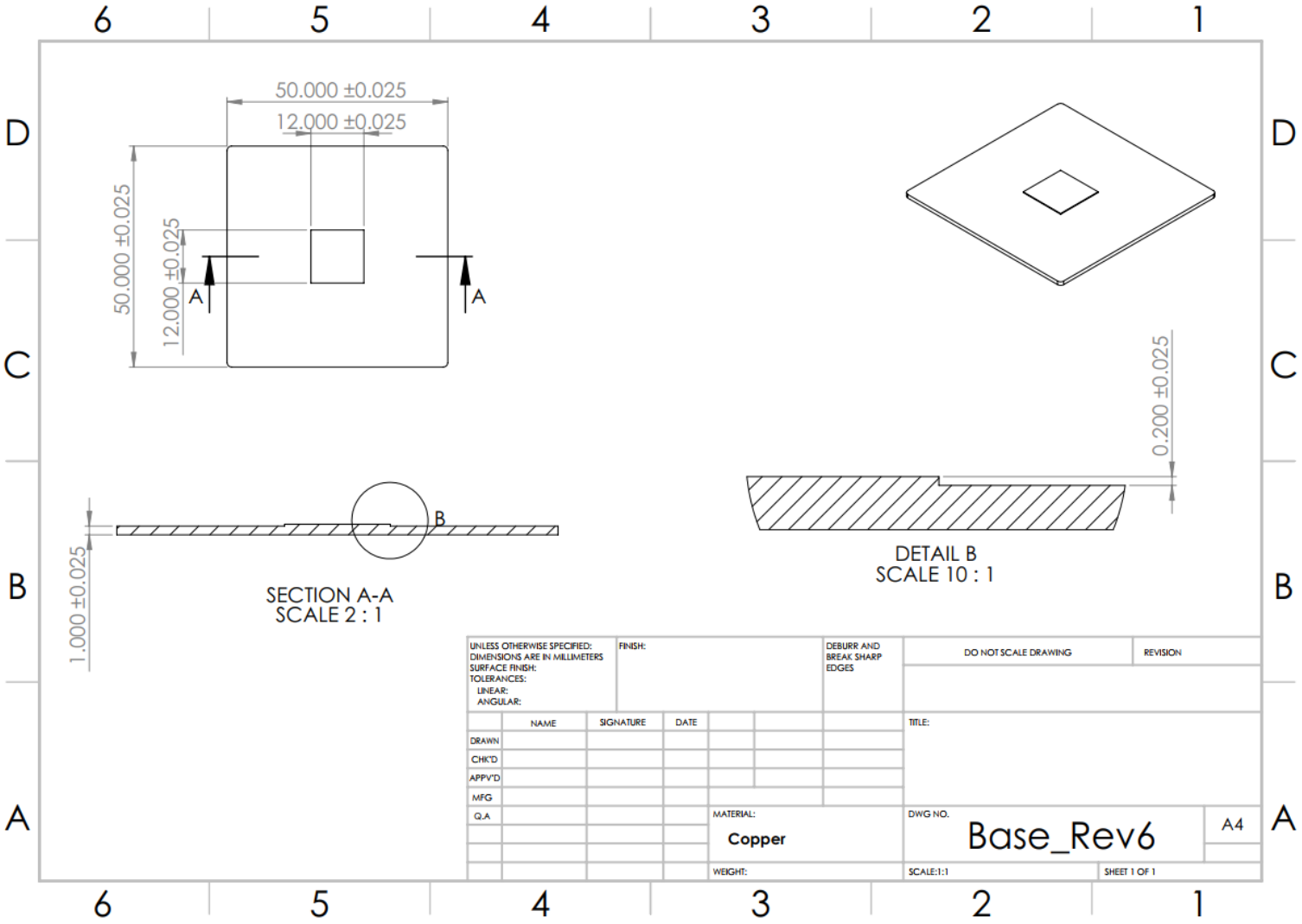

Figure B.6. Mechanical drawing of copper base.

B.5. Bottom Carrier Plate Drawings

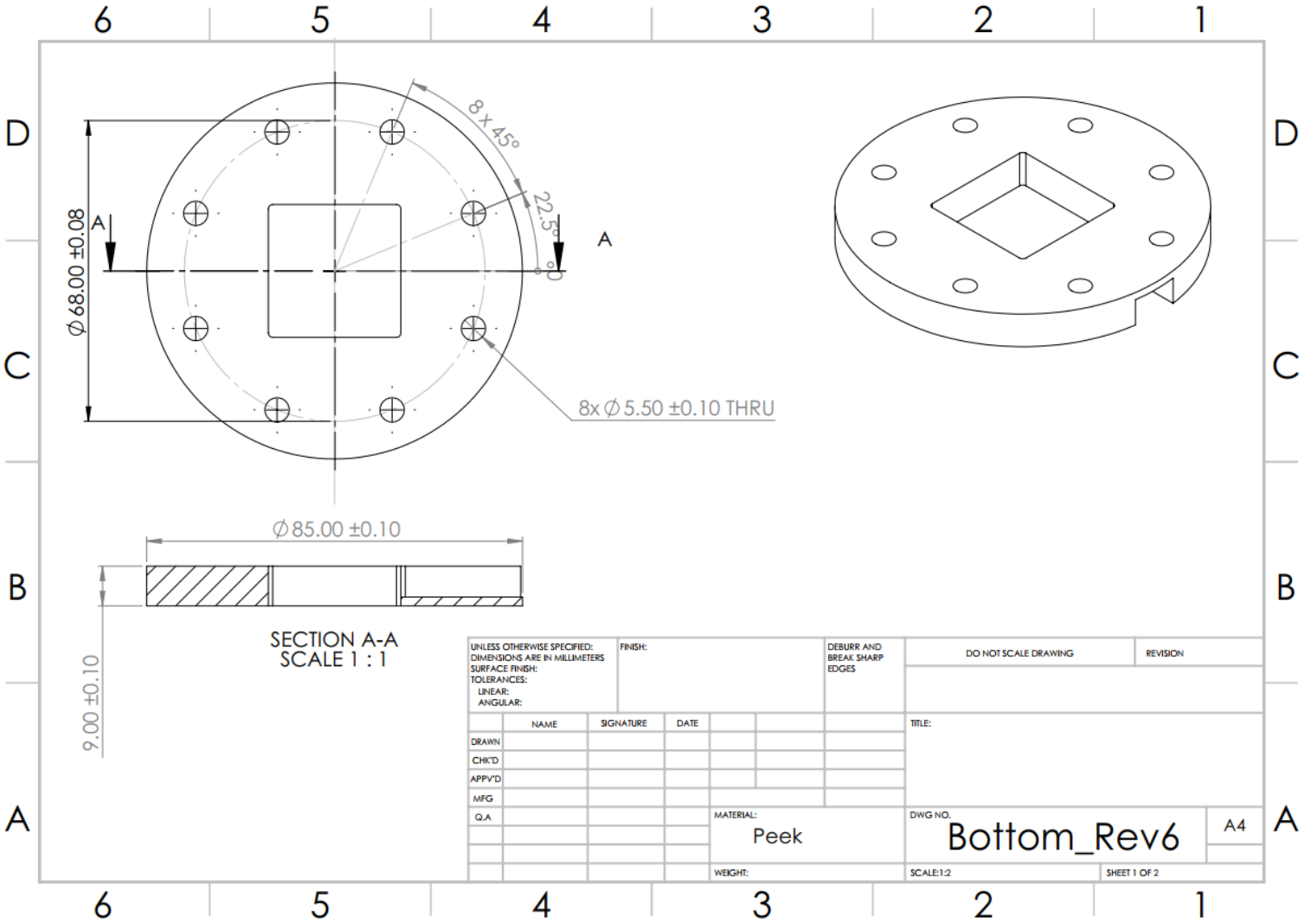

Figure B.7. Page 1/2 for the mechanical drawing of bottom carrier plate.

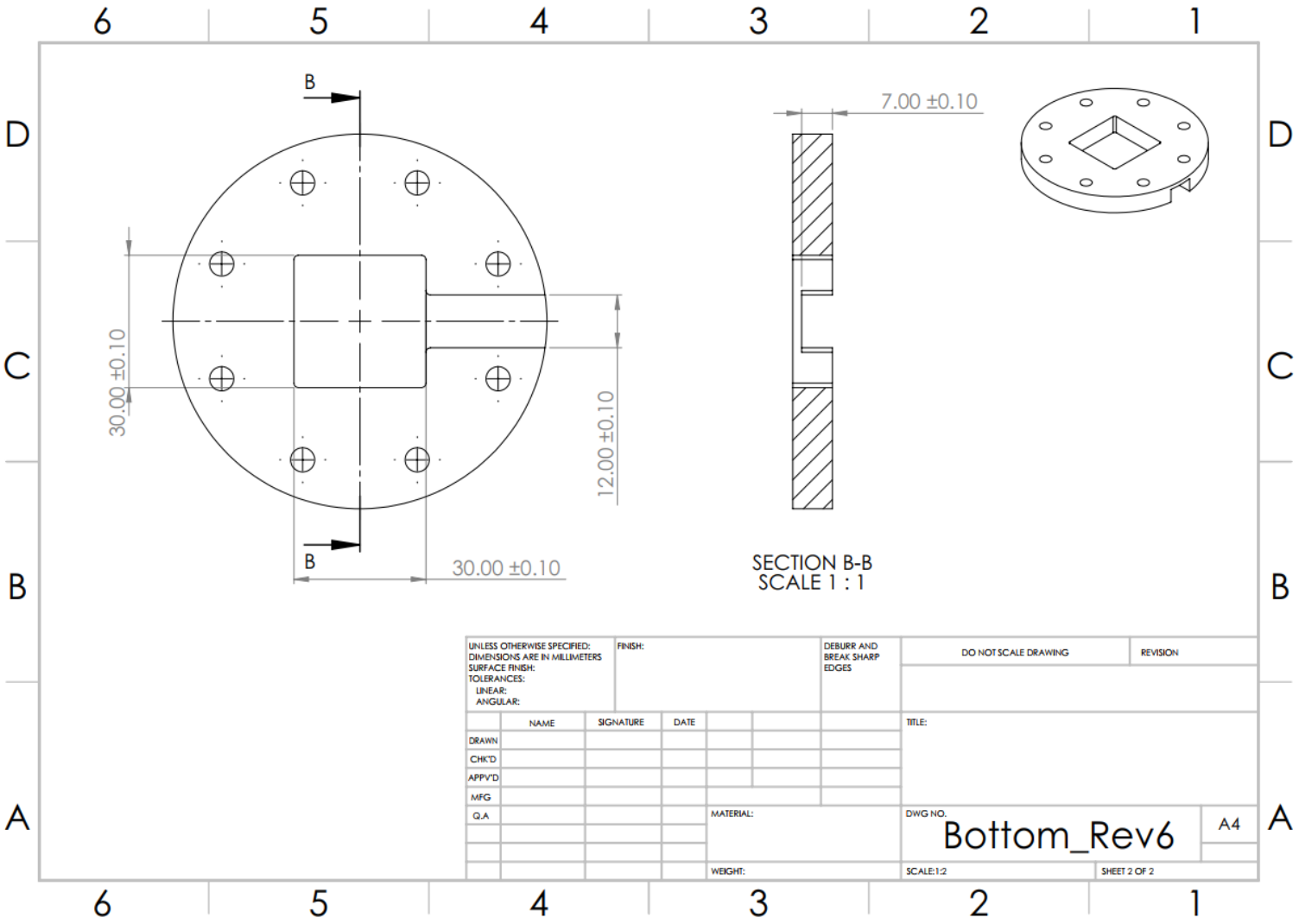

Figure B.8. Page 2/2 for the mechanical drawing of bottom carrier plate.

REFERENCES

[1] E. Laloya, Ó. Lucía, H. Sarnago, and J. M. Burdío, "Heat Management in Power Converters: From State of the Art to Future Ultrahigh Efficiency Systems," *IEEE Trans. Power Electron.*, vol. 31, no. 11, pp. 7896–7908, Nov. 2016.

[2] S. V Garimella, T. Persoons, and J. A. Weibel, "Electronics Thermal Management in Information and Communications Technologies: Challenges and Future Directions," 2017.

[3] J. Gullbrand, M. J. Luckeroth, M. E. Sprenger, and C. Winkel, "Liquid Cooling of Compute System," *J. Electron. Packag.*, vol. 141, no. 1, Mar. 2019.

[4] P. Rodgers, V. Eveloy, and M. G. Pecht, "Limits of air-cooling: Status and challenges," in *Annual IEEE Semiconductor Thermal Measurement and Management Symposium*, 2005, pp. 116–124.

[5] W. Nakayama, "Exploring the Limits of Air Cooling," |*Electronics Cooling*, 2006. [Online]. Available: https://www.electronics-cooling.com/2006/08/exploring-the-limits-of-air-cooling/. [Accessed: 25-Jul-2021].

[6] P. Rodgers, V. Eveloy, and M. G. Pecht, "Extending the limits of air-cooling in microelectronic equipment," in *Proceedings of the 6th International Conference on Thermal, Mechanical and Multi-Physics Simulation and Experiments in Micro-Electronics and Micro-Systems - EuroSimE 2005*, 2005, vol. 2005, pp. 695–702.

[7] McKinsey & Company, "Automotive revolution-perspective towards 2030," 2016.

[8] G. Xia, L. Cao, and G. Bi, "A review on battery thermal management in electric vehicle application," *Journal of Power Sources*, vol. 367. Elsevier B.V., pp. 90–105, 2017.

[9] A. R. M. Siddique, S. Mahmud, and B. Van Heyst, "A comprehensive review on a passive (phase change materials) and an active (thermoelectric cooler) battery thermal management system and their limitations," *Journal of Power Sources*, vol. 401. Elsevier B.V., pp. 224–237, 15-Oct-2018.

[10] M. A. Ebadian and C. X. Lin, "A Review of High-Heat-Flux Heat Removal Technologies," *J. Heat Transfer*, vol. 133, no. 11, p. 110801, 2011.

[11] B. Agostini, M. Fabbri, J. E. Park, L. Wojtan, J. R. Thome, and B. Michel, "State of the Art of High Heat Flux Cooling Technologies," *Heat Transf. Eng.*, vol. 28, no. 4, pp. 258–281, Apr. 2007.

[12] S. M. Sohel Murshed and C. A. Nieto de Castro, "A critical review of traditional and emerging techniques and fluids for electronics cooling," *Renewable and Sustainable Energy Reviews*, vol. 78. Elsevier Ltd, pp. 821–833, 01-Oct-2017.

[13] J. A. Weibel and S. V. Garimella, “Recent Advances in Vapor Chamber Transport Characterization for High-Heat-Flux Applications,” in *Advances in Heat Transfer*, vol. 45, Academic Press, 2013, pp. 209–301.

[14] I. Setyawan, N. Putra, and I. I. Hakim, “Experimental investigation of the operating characteristics of a hybrid loop heat pipe using pump assistance,” *Appl. Therm. Eng.*, vol. 130, pp. 10–16, 2018.

[15] Y. Peles, “Ledinegg (or Flow Excursion) Instability,” in *Contemporary Perspectives on Flow Boiling Instabilities in Microchannels and Minichannels*, S. G. Kandlikar, Ed. New York: Begell House, Inc, 2012, pp. 53–64.

[16] T. Van Oevelen, J. A. Weibel, and S. V. Garimella, “Predicting two-phase flow distribution and stability in systems with many parallel heated channels,” *Int. J. Heat Mass Transf.*, vol. 107, pp. 557–571, 2017.

[17] T. A. Kingston, J. A. Weibel, and S. V. Garimella, “Ledinegg instability-induced temperature excursion between thermally isolated, heated parallel microchannels,” *Int. J. Heat Mass Transf.*, vol. 132, pp. 550–556, Apr. 2019.

[18] A. Miglani, J. A. Weibel, and S. V Garimella, “Measurement of flow maldistribution induced by the Ledinegg instability during boiling in thermally isolated parallel microchannels,” *Int. J. Multiph. Flow*, vol. 139, p. 103644, 2021.

[19] F. Liu, Z. Yang, B. Zhang, and T. Li, “Study on Ledinegg instability of two-phase boiling flow with bifurcation analysis and experimental verification,” *Int. J. Heat Mass Transf.*, vol. 147, p. 118954, Feb. 2020.

[20] T. A. Kingston, J. A. Weibel, and S. V. Garimella, “High-frequency thermal-fluidic characterization of dynamic microchannel flow boiling instabilities: Part 1 – Rapid-bubble-growth instability at the onset of boiling,” *Int. J. Multiph. Flow*, vol. 106, pp. 179–188, Sep. 2018.

[21] C. J. Kuo and Y. Peles, “Flow boiling instabilities in microchannels and means for mitigation by reentrant cavities,” *J. Heat Transfer*, vol. 130, no. 7, Jul. 2008.

[22] Q. Jin, J. T. Wen, and S. Narayanan, “Characteristics of pressure drop oscillation in a microchannel cooling system,” *Appl. Therm. Eng.*, vol. 160, p. 113849, Sep. 2019.

[23] M. D. Clark, J. A. Weibel, S. V. Garimella, and S. V. Garimella, “Impact of Pressure Drop Oscillations on Surface Temperature and Critical Heat Flux during Flow Boiling in a Microchannel,” *IEEE Trans. Components, Packag. Manuf. Technol.*, pp. 1–1, 2021.

[24] H. Grzybowski and R. Mosdorf, “Dynamics of pressure drop oscillations during flow boiling inside minichannel,” *Int. Commun. Heat Mass Transf.*, vol. 95, pp. 25–32, Jul. 2018.

[25] C. Li, G. P. Peterson, and Y. Wang, “Evaporation/Boiling in Thin Capillary Wicks (I) - Wick Thickness Effects,” *J. Heat Transfer*, vol. 128, no. 12, pp. 1312–1319, 2006.

[26] C. Li and G. P. Peterson, “Evaporation/Boiling in Thin Capillary Wicks (II)-Effects of Volumetric Porosity and Mesh Size,” *J. Heat Transfer*, vol. 128, no. 12, pp. 1320–1328, 2006.

[27] S. Sudhakar, J. A. Weibel, and S. V. Garimella, “An area-scalable two-layer evaporator wick concept for high-heat-flux vapor chambers,” *Proc. 16th Intersoc. Conf. Therm. Thermomechanical Phenom. Electron. Syst. ITherm 2017*, pp. 537–546, 2017.

[28] M. Nikitkin and B. Cullimore, “CPL and LHP technologies: What are the differences, what are the similarities?,” *SAE Tech. Pap.*, vol. 107, no. 1998, pp. 400–408, 1998.

[29] M. Nishikawara, K. Otani, Y. Ueda, and H. Yanada, “Liquid–vapor phase behavior and operating characteristics of the capillary evaporator of a loop heat pipe at start-up,” *Int. J. Therm. Sci.*, vol. 129, pp. 426–433, 2018.

[30] C. Jiang, W. Liu, Z. Liu, J. Yang, B. Duan, and X. Luo, “Startup characteristics of pump-assisted capillary phase change loop,” *Appl. Therm. Eng.*, vol. 126, pp. 1115–1125, 2017.

[31] M. A. Chernysheva, Y. F. Maydanik, and J. M. Ochterbeck, “Heat Transfer Investigation in Evaporator of Loop Heat Pipe During Startup,” 2008.

[32] B. J. Huang, H. H. Huang, and T. L. Liang, “System dynamics model and startup behavior of loop heat pipe,” *Appl. Therm. Eng.*, vol. 29, pp. 2999–3005, 2009.

[33] B. Siedel, V. Sartre, and F. Lefèvre, “Literature review: Steady-state modelling of loop heat pipes,” *Appl. Therm. Eng.*, vol. 75, pp. 709–723, 2015.

[34] S. Launay and M. Vallée, “State-of-the-Art Experimental Studies on Loop Heat Pipes,” *Front. Heat Pipes*, vol. 2, no. 1, 2011.

[35] M. Crepinsek and C. Park, “Effect of operational conditions on cooling performance of pump-assisted capillary-driven two-phase loop,” *J. Thermophys. Heat Transf.*, vol. 25, no. 4, pp. 572–580, 2011.

[36] M. Crepinsek and C. Park, “Experimental analysis of pump-assisted and capillary-driven dual-evaporators two-phase cooling loop,” *Appl. Therm. Eng.*, vol. 38, pp. 133–142, 2012.

[37] M. Lee and C. Park, “Mechanical-capillary-driven two-phase loop: Numerical modeling and experimental validation,” *Int. J. Heat Mass Transf.*, vol. 125, pp. 972–982, 2018.

[38] F. P. Incropera, D. P. Dewitt, T. L. Bergman, and A. S. Lavine, *Principles of Heat and Mass Transfer*, Seventh Ed. Wiley, 2003.

[39] G. P. Peterson, “Other Operating Limits,” in *An Introduction to Heat Pipes. Modeling, Testing and Applications*, 1994, pp. 77–122.

[40] G. F. Smirnov, “Approximate Theory of Heat Transfer with Boiling on Surfaces Covered with Capillary-Porous Structures,” *Teploenergetika*, vol. 24, no. 9, pp. 77–80, 1977.

[41] R. Ranjan, J. Y. Murthy, and S. V. Garimella, “Bubble dynamics during capillary-fed nucleate boiling in porous media,” *Intersoc. Conf. Therm. Thermomechanical Phenom. Electron. Syst. ITHERM*, pp. 1114–1126, 2012.

[42] J. A. Weibel, S. V Garimella, M. T. North, J. A. Weibel, S. V Garimella, and M. T. North, “Characterization of Evaporation and Boiling from Sintered Powder Wicks Fed by Capillary Action,” 2010.

[43] J. A. Weibel, S. S. Kim, T. S. Fisher, and S. V. Garimella, “Carbon Nanotube Coatings for Enhanced Capillary-Fed Boiling from Porous Microstructures,” *Nanoscale Microscale Thermophys. Eng.*, vol. 16, pp. 1–17, 2012.

[44] C. Zhang *et al.*, “Enhanced Capillary-Fed Boiling in Copper Inverse Opals via Template Sintering,” *Adv. Funct. Mater.*, pp. 1–8, 2018.

[45] C. Zhang, J. W. Palko, M. T. Barako, M. Asheghi, and K. E. Goodson, “Design and optimization of well-ordered microporous copper structure for high heat flux cooling applications,” *Int. J. Heat Mass Transf.*, vol. 173, p. 121241, 2021.

[46] C. Zhang, J. W. Palko, M. T. Barako, M. Asheghi, J. G. Santiago, and K. E. Goodson, “Enhanced Capillary-Fed Boiling in Copper Inverse Opals via Template Sintering,” *Adv. Funct. Mater.*, vol. 28, no. 41, pp. 1–8, 2018.

[47] C. Zhang, J. W. Palko, M. T. Barako, M. Asheghi, J. G. Santiago, and K. E. Goodson, “Enhanced Capillary-Fed Boiling in Copper Inverse Opals via Template Sintering,” *Adv. Funct. Mater.*, vol. 28, no. 41, Oct. 2018.

[48] S. Sudhakar, J. A. Weibel, and S. V. Garimella, “Design of an area-scalable two-layer evaporator wick for high-heat-flux vapor chambers,” *IEEE Trans. Components, Packag. Manuf. Technol.*, vol. 9, no. 3, pp. 458–472, 2019.

[49] S. Sudhakar, J. A. Weibel, and S. V. Garimella, “Experimental investigation of boiling regimes in a capillary-fed two-layer evaporator wick,” *Int. J. Heat Mass Transf.*, vol. 135, pp. 1335–1345, 2019.

[50] S. Sudhakar, J. A. Weibel, F. Zhou, E. M. Dede, and S. V. Garimella, “The role of vapor venting and liquid feeding on the dryout limit of two-layer evaporator wicks,” *Int. J. Heat Mass Transf.*, vol. 148, p. 119063, 2020.

[51] C. Park, A. Vallury, and J. Zuo, “Performance evaluation of a pump-assisted, capillary two-phase cooling loop,” *J. Therm. Sci. Eng. Appl.*, vol. 1, no. 2, pp. 1–8, 2009.

[52] K. K. Bodla, J. Y. Murthy, and S. V. Garimella, “Direct Simulation of Thermal Transport Through Sintered Wick Microstructures,” *J. Heat Transfer*, vol. 134, 2012.

[53] F. Zhou, S. N. Joshi, Y. Liu, and E. M. Dede, “Near-junction cooling for next-generation power electronics,” *Int. Commun. Heat Mass Transf.*, vol. 108, Nov. 2019.

[54] W. E. Frazier, “Metal Additive Manufacturing: A Review,” *J. Mater. Eng. Perform.*, vol. 23, pp. 1917–1928, 2014.

[55] D. Herzog, V. Seyda, E. Wycisk, and C. Emmelmann, “Additive manufacturing of metals,” *Acta Mater.*, vol. 117, pp. 371–392, 2016.

[56] C. Buchanan and L. Gardner, “Metal 3D printing in construction: A review of methods, research, applications, opportunities and challenges,” *Engineering Structures*, vol. 180. Elsevier Ltd, pp. 332–348, 01-Feb-2019.